UCRL-17605

cy. 2

University of California

Ernest O. Lawrence Radiation Laboratory

π^--He^4 INELASTIC AND CAPTURE REACTIONS LEADING TO EXCITED AND MULTI-NEUTRON FINAL STATES

Leon Kaufman

(Ph. D. Thesis)

August 1, 1967

TWO-WEEK LOAN COPY

This is a Library Circulating Copy which may be borrowed for two weeks. For a personal retention copy, call Tech. Info. Division, Ext. 5545

Berkeley, California

UCRL-17605 cy. 2

DISCLAIMER

This document was prepared as an account of work sponsored by the United States Government. While this document is believed to contain correct information, neither the United States Government nor any agency thereof, nor the Regents of the University of California, nor any of their employees, makes any warranty, express or implied, or assumes any legal responsibility for the accuracy, completeness, or usefulness of any information, apparatus, product, or process disclosed, or represents that its use would not infringe privately owned rights. Reference herein to any specific commercial product, process, or service by its trade name, trademark, manufacturer, or otherwise, does not necessarily constitute or imply its endorsement, recommendation, or favoring by the United States Government or any agency thereof, or the Regents of the University of California. The views and opinions of authors expressed herein do not necessarily state or reflect those of the United States Government or any agency thereof or the Regents of the University of California.

UCRL-17605

UNIVERSITY OF CALIFORNIA

Lawrence Radiation Laboratory
Berkeley, California

AEC Contract No. W-7405-eng-48

π^--He^4 INELASTIC AND CAPTURE REACTIONS LEADING TO EXCITED AND MULTI-NEUTRON FINAL STATES

Leon Kaufman
(Ph. D. Thesis)

August 1, 1967

π^--He^4 INELASTIC AND CAPTURE REACTIONS LEADING TO EXCITED AND MULTI-NEUTRON FINAL STATES

Contents

Abstract vii

I. Introduction

A. Three-Neutron System 1

B. Four-Neutron System 2

C. Excited States of He^4 3

II. Experimental Method and Apparatus

A. Introduction. 5

B. Experimental Layout 9

C. Beam 10

D. Target. 17

E. Spectrometer

1. Physical Setup 18

2. Particle Discrimination 20

F. Electronics

1. Logic Requirements. 22

2. Logic Acquisition 24

G. Running Conditions. 28

III. Data Analysis

A. General Analysis

1. Determination of Fiducial Distances 29

2. Finding the Spark Coordinates 29

3. Determination of a Point. 30

4. A Line is Born. 31

5. Target Check. 31

6. Matching the Lines 31

7. Calculation of the Momentum. 32

8. Event-Acceptance Criteria. 32

9. Corrections to the Data. 36

10. The Last Step. 42

B. Error Estimates

1. Scattering in the Spectrometer 44

2. Determination of the Scattering Angle in the Target. 49

3. Determination of the Point of Intersection in the Target 50

4. Energy Resolution. 50

IV. Results

A. $\pi^- + He^4$ and $\pi^- + He^{4*}$ Channels. 51

B. $\pi^+ + 4n$ Channel. 51

C. $p + 3n$ Channel 51

D. $d + 2n$ Channel 56

V. Interpretation and Conclusions

A. $\pi^- + He^{4*}$ Channel. 57

B. $d + 2n$ Channel 58

C. $p + 3n$ Channel 58

D. $\pi^+ + 4n$ Channel. 64

Acknowledgments 65

Appendices

A. Magnetostrictive Readout Chambers. 67

1. Construction 67

2. Chamber Performance

a. Accuracy 69

b. Efficiency. 71

B. Reduction and Recording of Magnetostrictive-Readout Chamber Data. 77

References 83

π^--He^4 INELASTIC AND CAPTURE REACTIONS LEADING TO EXCITED AND MULTI-NEUTRON FINAL STATES

Leon Kaufman

Lawrence Radiation Laboratory
University of California
Berkeley, California

ABSTRACT

A beam of 140 $\pm$0.5-MeV π^- was produced at the Berkeley 184-inch cyclotron and used to study the final-state interactions of three and four neutrons, and to look for excited levels of the α particle through the reactions:

$$\pi^- + He^4 \rightarrow \pi^- + He^{4*}$$
$$\rightarrow p + 3n$$
$$\rightarrow d + 2n$$
$$\rightarrow \pi^+ + 4n.$$

Only one such level is found, with an excitation energy of 32 MeV and an intrinsic width smaller than our 1-MeV resolution. We find that our data on the four-neutron final state is best fit by considering two neutrons interacting through a $^1S_0$ potential, and the two other ones as spectators. We find too that deuteron production is down by a factor of $\sim 10^3$ from proton production, and that the proton spectrum shows a stronger than expected interaction between the three neutrons in the final state.

Lower limits for the production of a tri or tetraneutron are set.

I. INTRODUCTION

The n-n interaction at low energies has been extensively studied through reactions such as $D(n,p)2n$,[1] $H^3(n,d)2n$,[2] and $T(d,He^3)2n$;[3] and through a different approach by the reaction $\pi^- + D \rightarrow 2n + \gamma$,[4] where in the final state only the two neutrons are strongly interacting. The theory for the analysis of the data obtained in these experiments is quite well known and has almost become a textbook problem.[3,5-7]

On the other hand, data on the three- and four-neutron systems is scarce and inadequate, and theoretical predictions are contradicting and inconclusive.

A. Three-Neutron System

The n^3 has been searched for through the reaction $H^3(n,p)3n$. In 1965 Ajdacic et al. reported observing a proton distribution of energy that led to an n^3 bound by about 1 MeV.[8] This experiment was repeated later at Oak Ridge National Laboratory,[9] and no evidence for the existence of the n^3 system was observed.

A paper by Mitra and Bhasin[10] predicts the existence of the n^3. They argue that only a moderate ^3P attractive force is needed between all neutron pairs to yield a bound n^3 system, and they predict an (LSJ) = (1, 3/2, 1/2) state as the most likely, with a second best (1, 3/2, 3/2). Mitra and Bhasin comment that the existence of the n^3 is independent of the n^4, for in the latter the $^1S_0$ repulsive interaction plays the bigger role, while such a force is negligible in the n^3 case.

It is worthwhile noting that the rule of Baz', Goldanskii, and Zel'dovich, which states that the binding energy of the (2m + 2)th neutron is always greater than the binding energy of the (2m + 1)th neutron, and which would tie the nonexistence of n^3 with the nonexistence of n^4, does

not necessarily apply to the lightest nuclei, for it is derived from shell-model considerations.

Okamoto and Davies[11] assume a (1, 3/2, 1/2) state too, but obtain an n^3 state unbound by about 10 MeV. They use potentials with parameters consistent with the known H^3 and He^3 data. They point out that light neutron nuclei should be unbound too from the systematics of nuclei with n = 3 and n = 2.

Phillips arrives at an unbound n^3 using the Faddeev equations and what is known of the two-nucleon interactions.[12] All of these authors make the drastic assumption that the interactions in the three-nucleon systems are due to a combination of pair interactions. As pointed out by Noyes,[13] these approaches are not far enough along to show if experimental data can be interpreted purely in this way or if actual three-body forces exist.

B. Four-Neutron System

The n^4 has been searched for by looking for its signature in medium-weight nuclei breakup,[14] or light nuclei breakup such as $\pi^- + Li^7 \rightarrow n^4 + He^3$.[15,16] (In this same experiment detection of the reaction $\pi^- + Li^7 \rightarrow H^3 + H^4$,[15] with T = 1 or T = 2 for the H^4, was also reported.)

Another approach has been to observe the effects of the interactions of the four neutrons on the phase space of one observed particle. Such an experiment can shed light not only on the existence of a bound state, but also on the actual interactions between the neutrons.

The reaction studied was $\pi^- + He^4 \rightarrow \pi^+ + 4n$.[17,18] No n^4 was found and the CERN group[18] that performed this experiment finds a phase space for the π^+ that leads to a final-state interaction between <u>two neutrons only</u>. The resolution in this experiment was an order of magnitude

larger than the expected binding energy of the n^4, and therefore the results are not conclusive.

Tang and Bayman predict that two dineutron clusters will not be bound, and further, that the relative energy of the dineutron clusters goes down monotonically as a function of increasing radius.[19] This would lead one to believe that no n^4 resonance exists either. They use for their calculation the n-n singlet-even potential and a triplet-odd potential assumed to be zero except for a hard core of small radius. These authors point out that inclusion of a weak attractive potential in the triplet-odd state does not change their conclusion.

The question of the n^4 is tied directly with excited states of He^4, and a review of this field is of consequence.

C. Excited States of He^4

The literature abounds with experimental data and theoretical analysis on the He^4 nucleus.[20-29] An adequate review is afforded by Argan et al.[29] They summarize what is known about the problem as follows. One can believe either:

1. a. The triplet ^4H - $^4He^*$ - ^4Li exists,[15,30,31] with E ~ 24 MeV, and T = 1.

   b. The reported levels at 21 and 22 MeV are the same with T = 0. They could represent the $P_{3/2}$-$P_{1/2}$ spin orbit splitting, but then a T = 1 value would be expected as above. For such a T value excited states of Li^4 and H^4 should exist at ~ 22 MeV. Experimentally they have not been seen.

   c. There exists a T = 2 state at 30 MeV.

   d. The 20-MeV level exists and has T = 0 or indefinite isospin.

Or, the authors consider further the possibility that:

2. The 20-, 24-, and 30-MeV levels are "quasi states,"[32] the only "true" level being the one at 22 MeV with T = 0. A second "true" state with ~ 24 MeV and T = 1 should exist.

They conclude with the observation that the present knowledge of the nuclear structure of He^4 is lacking and sometimes contradictory.

With this in mind we started to plan early in 1966 a "high-energy-type" experiment with high resolution. We noticed that the $\pi^- + He^4$ reaction, at a proper π^- energy, would allow us to study simultaneously three neutron forces through the p + 3n channel, four neutron interactions through the $\pi^+ + 4n$ channel, the excited states of He^4 with T = 0, 1, and 2 through the $\pi^- + He^{4*}$ channels. Of further interest was the d + 2n channel, for it would give an indication of the strength of the p-n interaction in the 4-body final state p- + 3n, yielding at the same time a value for the deuteron component of the α-particle wave function.

II. EXPERIMENTAL METHOD AND APPARATUS

A. Introduction

For π^- mesons (of energy less than necessary for production of a second π) on He^4 the following final-state channels are possible:

1. Elastic Scattering

$$\pi^- + He^4 \tag{1}$$

2. Inelastic Scattering

$$\pi^- + He^{4*} \tag{2}$$

$$\pi^- + n + He^3 \tag{3}$$

$$\pi^- + 2n + 2p \tag{4}$$

$$\pi^- + D + D \tag{5}$$

$$\pi^- + T + p \tag{6}$$

$$\pi^- + n + p + D \tag{7}$$

3. Charge Exchange

$$\pi^o + p + 3n \tag{8}$$

$$\pi^o + 2n + D \tag{9}$$

$$\pi^o + n + T \tag{10}$$

$$\pi^o + H^4 (?)^{15} \tag{11}$$

$\hookrightarrow 2\gamma$ or Dalitz pair + γ.

4. Absorption

$$p + 3n \tag{12}$$

$$D + 2n \tag{13}$$

$$T + n \tag{14}$$

5. Double Charge Exchange (DCX)

$$\pi^+ + 4n \tag{15}$$

Notice that for all channels mentioned in the previous section one particle in the final state is charged, and this affords an easy measurement of its momentum. The reactions of interest are: (1), for it allows us to check spectrometer calibration and affords a way to determine the energy and energy spread of the incoming beam; (2), for it can yield excited states of He^4 with T = 0, 1, and 2; (12), where the high-momentum end of the proton spectrum will reflect the final-state interactions of the neutrons with low relative energy; (13), the deuteron spectrum being distorted by the n-n interactions; (15), the phase-space distribution of the π^+ yields information on the final-state interactions of the four neutrons. The π^+-N interaction cross section is much smaller than the n-n cross section and does not affect the π^+ spectrum in an appreciable way.

Figure 1 shows the thresholds for the charged products of the above reactions calculated for an incoming π^- beam of 242 MeV/c (T = 140 MeV), the values being given for 20 deg in the lab system.

While reaction (1) will show a clean peak, the background from reactions (3) through (7) will overlap the region where we expect the π^- produced in reaction (2) ($Q_{(2)} \lesssim 40$ MeV).

The thresholds are 20.3, 28.0, 23.6, 19.5, and 21.7 MeV, respectively. Fortunately the π^- spectrum from each one of these reactions will not be peaked, but will follow the characteristic many-particle phase-space distributions. Therefore, we will have the possible peaks from (2) superimposed on a smoothly varying background.

The proton spectrum from (12) will be free of background from its threshold down to 450 MeV/c, and the deuteron spectrum likewise down to 575 MeV/c. Time-of-flight (TOF) measurements can easily separate protons from deuterons in this energy range, and tritium or helium nuclei

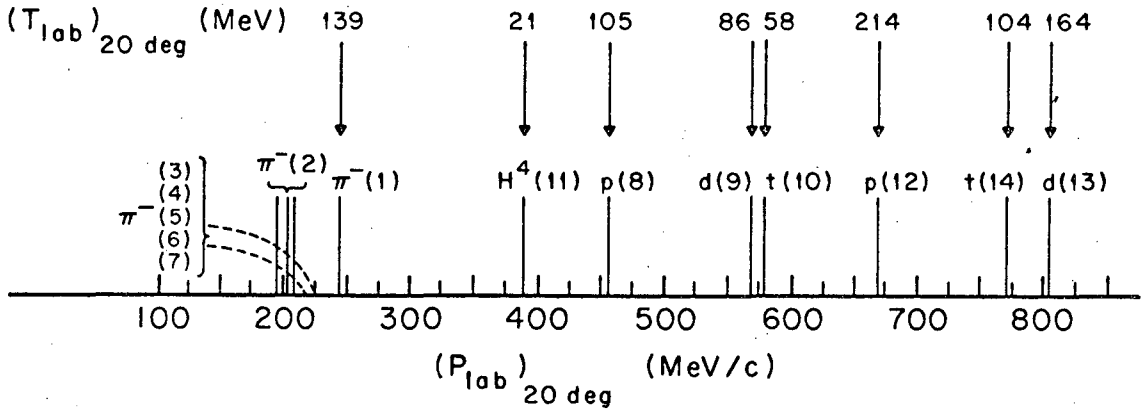

XBL676-3292

Fig. 1. Thresholds for selected channels in $\pi^- + He^4$. The number in parentheses indicates the reaction (as in Section II. A.) from which the particle originates. The protons from reactions (4), (6), and (7) have thresholds just below the proton threshold for reaction (8).

produced in the various reactions will either have too low an energy to go through our setup or will likewise be differentiated by TOF.

The background of positrons produced by pair conversion of the π^0 was calculated by a Monte Carlo method. We found that for our spectrometer only one positron would be detected for every 0.63×10^6 π^0's produced, and even though the ratio of total cross sections for processes (8) through (11) to the DCX cross section is not known, it certainly is no larger than $\sim 5 \times 10^2$. This would mean that e^+ background is negligible. The low-energy proton and deuteron background can easily be separated from the π^+'s, as will be seen later.

B. Experimental Layout

A 242 $\pm$0.50 MeV/c π^- beam was focused on a liquid-He^4 target, and the products of the reactions were momentum-analyzed at 20 deg in the laboratory (lab) system by a magnetic spectrometer, to be described later.

This particular beam energy was chosen because it allowed simultaneous analysis of the π^+, p, and D spectra at 20 deg using the maximum field attainable in our magnet (therefore, at maximum attainable resolution). The target exit angle of 20 deg was chosen as a compromise between the following:

1. Conditions that Favor a Small Angle

a. The higher lab cross section in the forward direction favors small angles.

b. The target image as seen by the spectrometer becomes smaller at small exit angles; therefore it allows for use of a longer target and higher yields.

2. Conditions Favoring a Large Angle

a. The exiting particle would have to go through a longer path in the He of the target if emitted at small angles, and any uncertainties in the knowledge of the point of interaction would be minimized at large (near 90 deg) angles.

b. Rutherford scattering drops as the angle increases.

Furthermore the Coulomb- and nuclear-scattered waves are expected to interfere destructively at this energy (the maximum cross section for 300-MeV π^- on He^4 occurs near 18 deg),[32] with a consequent drop in cross sections at small angles. Considerations of these factors led to choosing 20 deg for our exit angle.

C. Beam

The circulating 735-MeV proton beam of the 184-inch Berkeley cyclotron was allowed to strike an internal Be target. The resultant π^- were momentum-analyzed first by the cyclotron's own fringe field. This field can be approximated by a focusing lens, followed by a bending field and another focusing lens. The matrix elements corresponding to this combination were obtained by computing the orbits of not only the central, but also the off-axis, off-angle, and off-momentum rays. These, and the position of the internal target were calculated by the use of the program CYCLOTRON ORBITS,[33] This matrix was used when designing the optical conditions of the beam. For this purpose we used the program OPTIK.[34]

Our aim was to achieve a very monochromatic beam ($\Delta P \leq 1\%$), and for this a large amount of bending was necessary. The final configuration is shown in Fig. 2, where Q_1 is a doublet with an 8-in. bore that "collects" the beam and focuses its central elements at infinity, M_1 is a 29- by 36-in. magnet with an 8-in. gap where the beam undergoes a 90-deg bend, and Q_2 is a second doublet with a 12-in. bore which, together with the vertical effects due to M, focuses the beam on the target.

The currents to attain the desired focusing in Q_1 were determined by maximizing at the He target a 1-in.^{2} section of beam that was collimated between Q_1 and M_1 by a lead-brick counter combination.

The current in M_1 had been determined previously by the suspended-wire technique so as to yield the desired orbits for the central momentum. The currents in Q_2 were set then so as to maximize the momentum-analyzed beam at the target.

The beam was monitored by two sets of counters. A_1, A_2, A_3, A_4 were four 6- by 1.5- by 1/32-in. counters overlapped in pairs (A_1 and A_2,

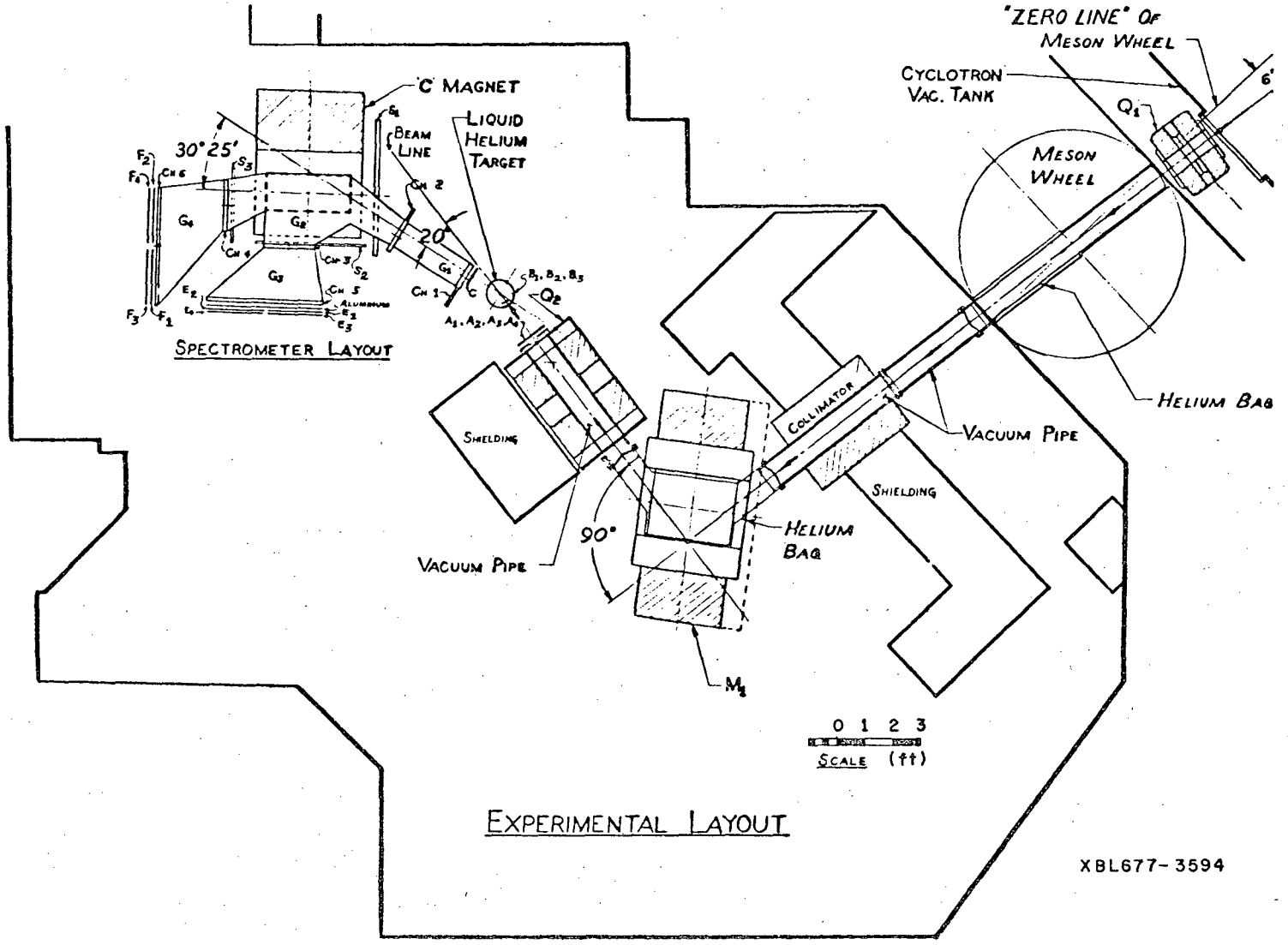

Fig. 2. Experimental layout.

A_3 and A_4) so as to yield 3/4-in. resolution. B_1, B_2, and B_3 were 2- by 0.5- by 1/32-in. and were overlapped so that they covered an 2- by 1-in. area, with 1/4-in. resolution.

To minimize scattering over this long beam line, a combination of He gas bags and vacuum pipes was used as shown in Fig. 2. Figure 3 shows the optical system. An integral range curve of the beam was taken by the use of Cu absorbers, and it was found that it consisted of 58 $\pm$ 10% π^-'s, 28% μ^-'s, and 14% e^-'s (Fig. 4).

At the particular energy of this beam, straggling will produce a 5% (FWHM) spread in energy. This is in agreement with the spread obtained from differentiating the range curve graphically, which yields 5% (Fig. 5).

For a finer determination of this quantity a thin (3/16-in.) carbon target was positioned at 45 deg to the beam, and the elastically scattered negative pions were momentum-analyzed by the spectrometer. The total spread observed was $\pm$ 0.50 MeV/c HWHM at 237 MeV/c. (No correction was made for energy loss in the target.) This allowed us also to check the calibration by detecting at the same time the first excited level of C^{12} at 4.4 MeV, as seen in Fig. 6.

Beam rates varied from 30 000/sec on Monday mornings after Sunday night shutdowns to 110 000/sec on Wednesday nights just before Thursday morning maintenance shutdowns.

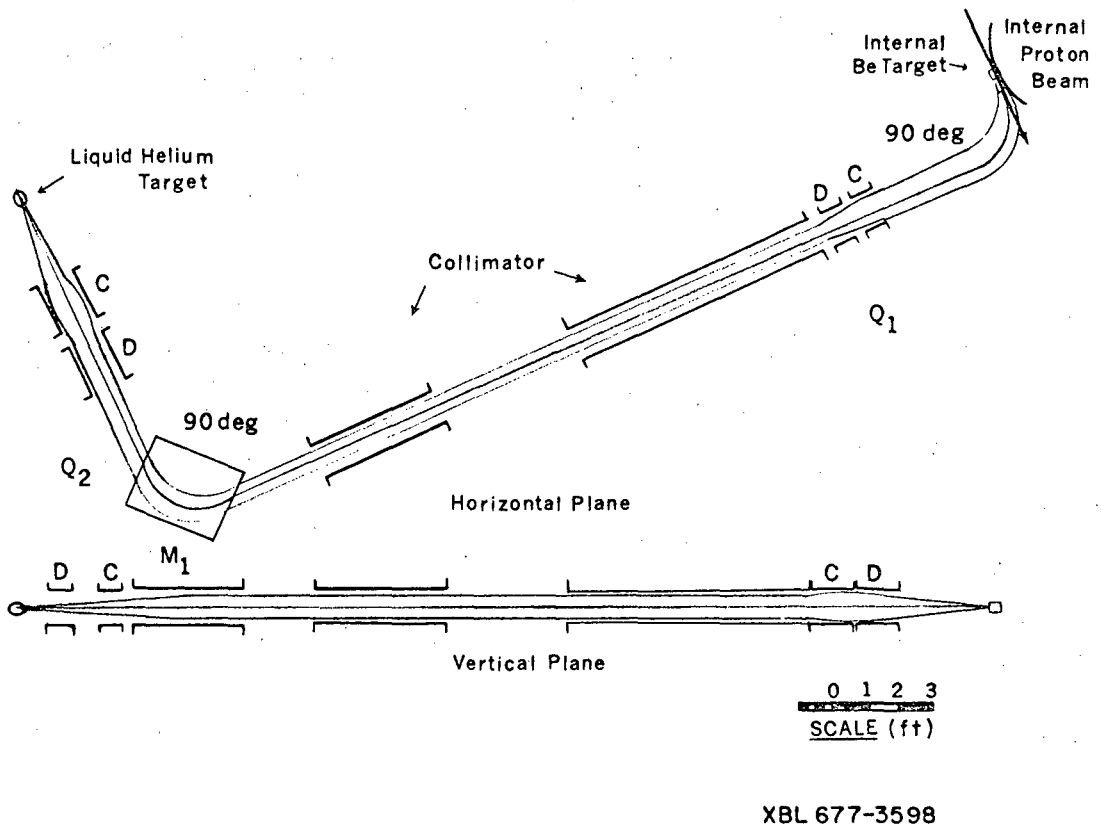

Fig. 3. Beam optics diagram.

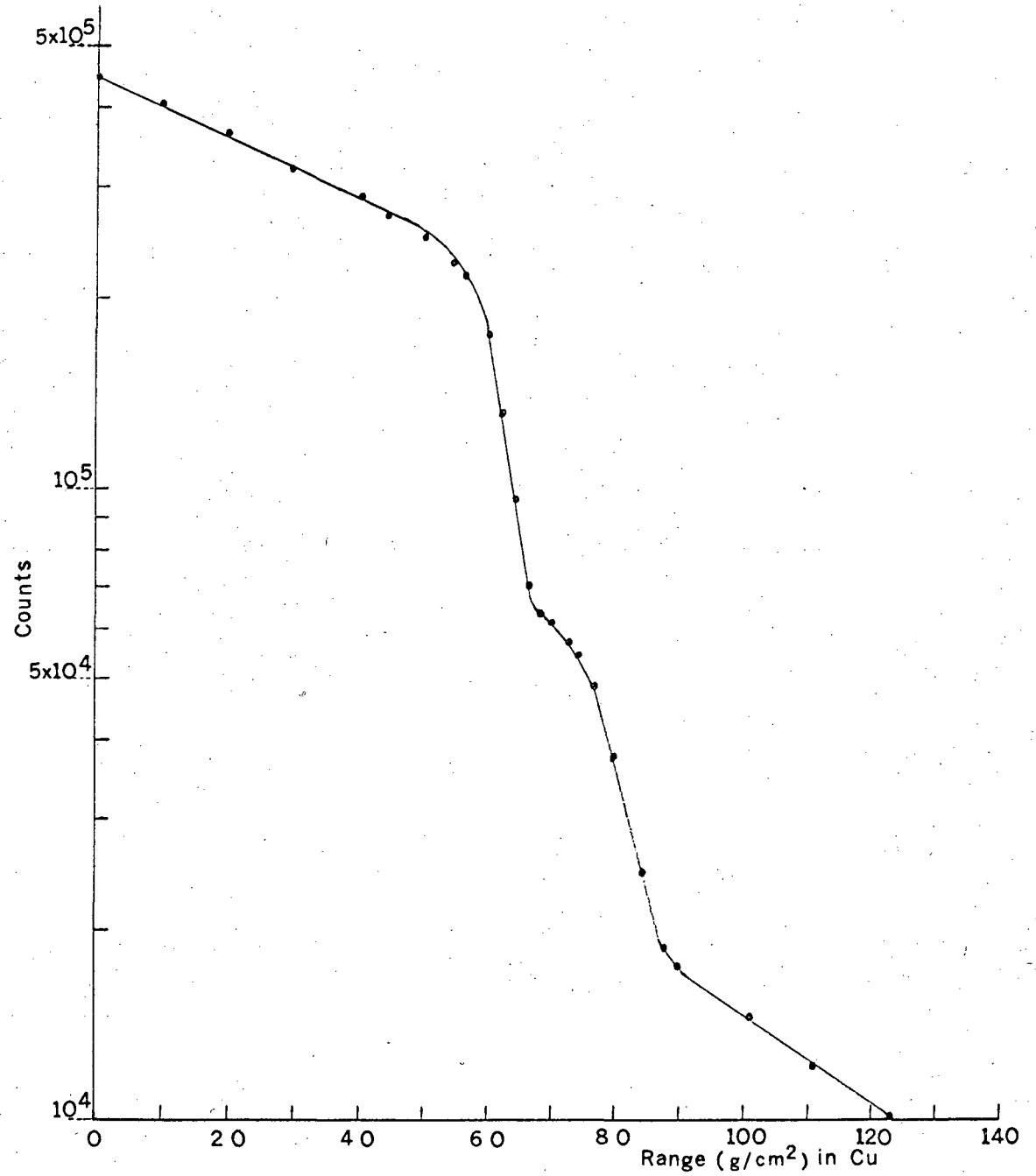

XBL 678-4403

Fig. 4. Integral beam range in Cu.

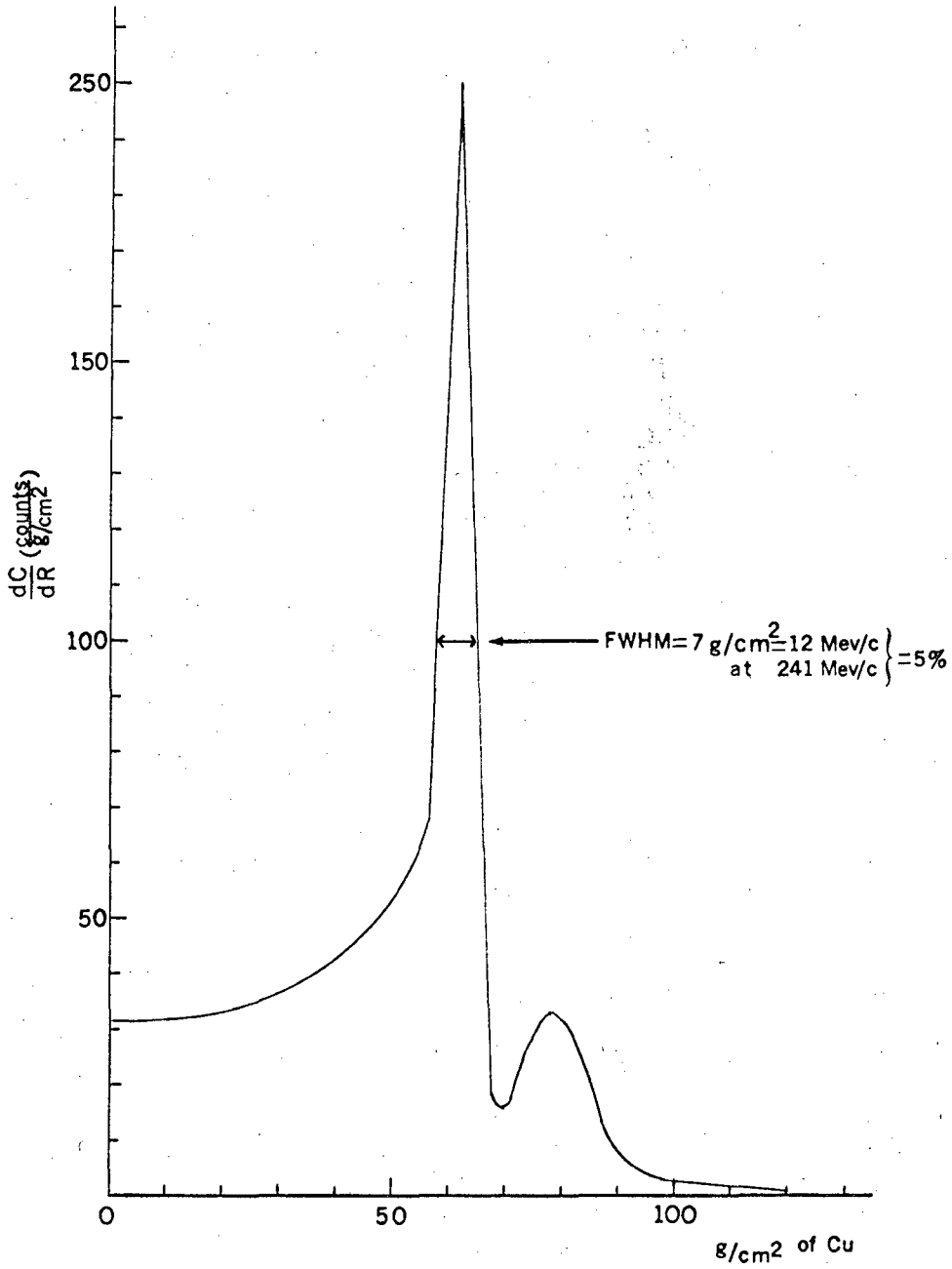

XBL 678-4402

Fig. 5. Differential range curve.

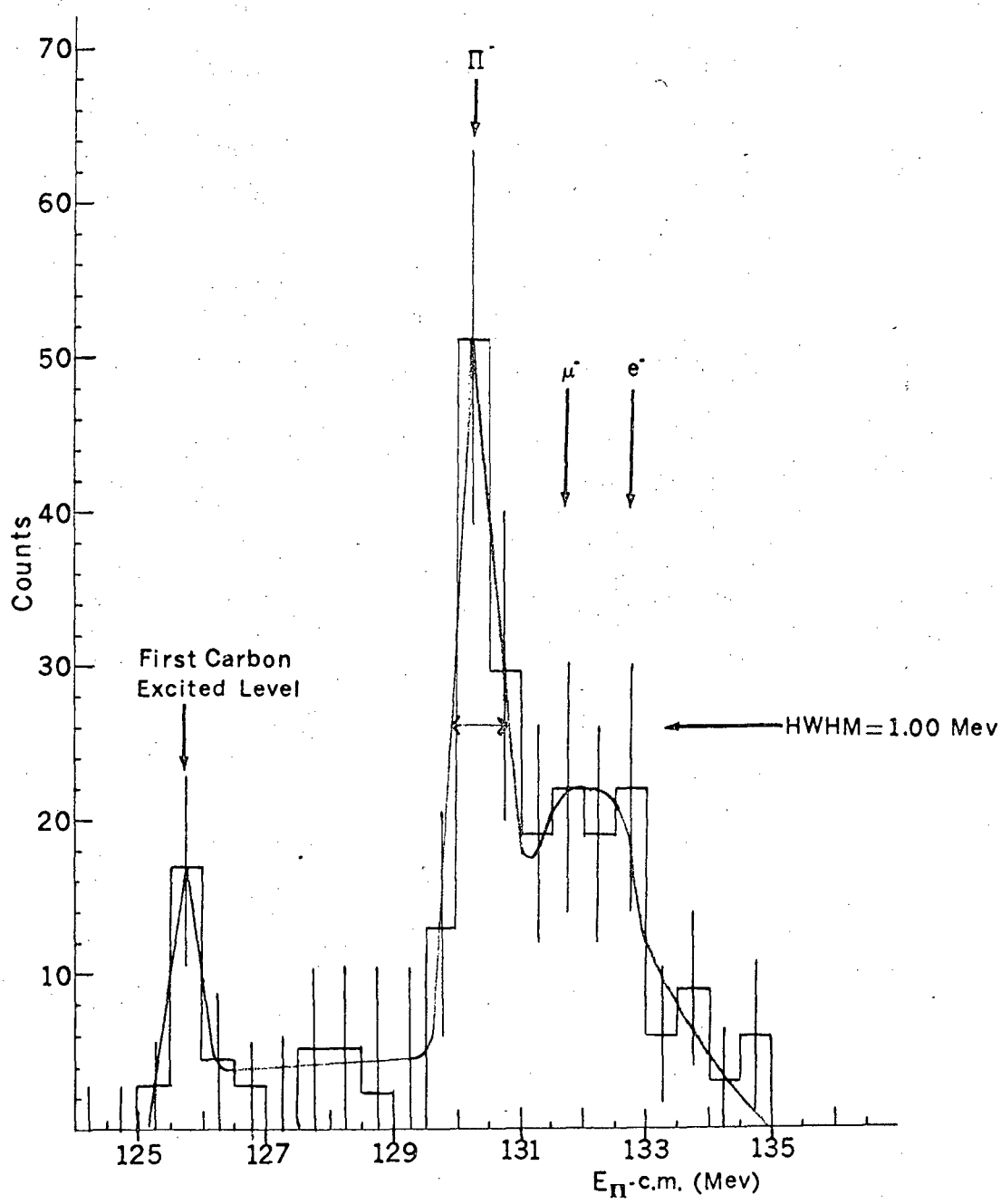

XBL 678-4401

Fig. 6. $\pi^- + C$ elastic-scattering spectrum.

D. Target

We used a 9- by 2- by 2-in. liquid-He flask, the long axis being parallel to the beam direction. The 2- by 2-in. sides, as well as the 2 by 9-in. side through which the scattered particles left the container, were 7.5-mil Mylar. This allowed for low-mass entrance and exit windows. The other three walls were aluminum. A liquid-N_2 jacket surrounded the three aluminum walls. The whole assembly was enclosed in three heat shields, each consisting of seven layers of 1/4-mil aluminized Mylar. This assembly was suspended from a liquid-He reservoir and enclosed in a cylindrical vacuum jacket with two 5-mil Mylar windows, one for the incoming beam and the other (larger) for the outgoing and scattered beams. A boil-off valve could be closed, and the pressure produced by either the evaporated He or gas admitted from an external source would force the liquid back into the reservoir when desired.

E. Spectrometer

1. Physical Setup

Figures 2 and 7 show the spectrometer layout. If the magnetic field, an entrance line, and an exit point are known in a particle's trajectory, the momentum of that particle is uniquely determined. If a second point on the exit path is known, the problem is overdetermined, and consistency can be checked for.

The field was produced by a 16- by 36-in. BeV "C" magnet with an 8-in. gap. A 2-in.-thick (S_1) iron shield with an 8-in. gap was provided to assure that no bending occurred in the particle's incoming path, and two 5/8-in. shields with 22- by 18-in. holes were added on the exit sides to reduce the extent of the magnet's stray field (S_2 and S_3).

The coordinates of the incoming track were determined by two 8- by 8-in. spark chambers (Chambers 1 and 2). By each side of the magnet we placed a 22- by 18-in. spark chamber (Chamber 3 or 4) followed by a 49- by 17-in. chamber (Chamber 5 or 6).

These chambers consisted of four planes of wires: two high-voltage (HV) central planes and two grounded outside ones. Each HV-ground pair was fired by a different capacitor. This decoupled each gap so that we effectively had two spark chambers in each assembly, with only the 90% Ne-10% He gas mixture flowing through the chamber in common. A small amount of ethyl alcohol was added to the gas to act as a spark quencher, and a 35-V clearing field was used to reduce the resolution time of the chambers.[35]

Data were collected by the magnetostrictive-readout method[36-39] onto magnetic tape. The output of each plane in the chambers consisted of a number for the spark position and another for the total length or

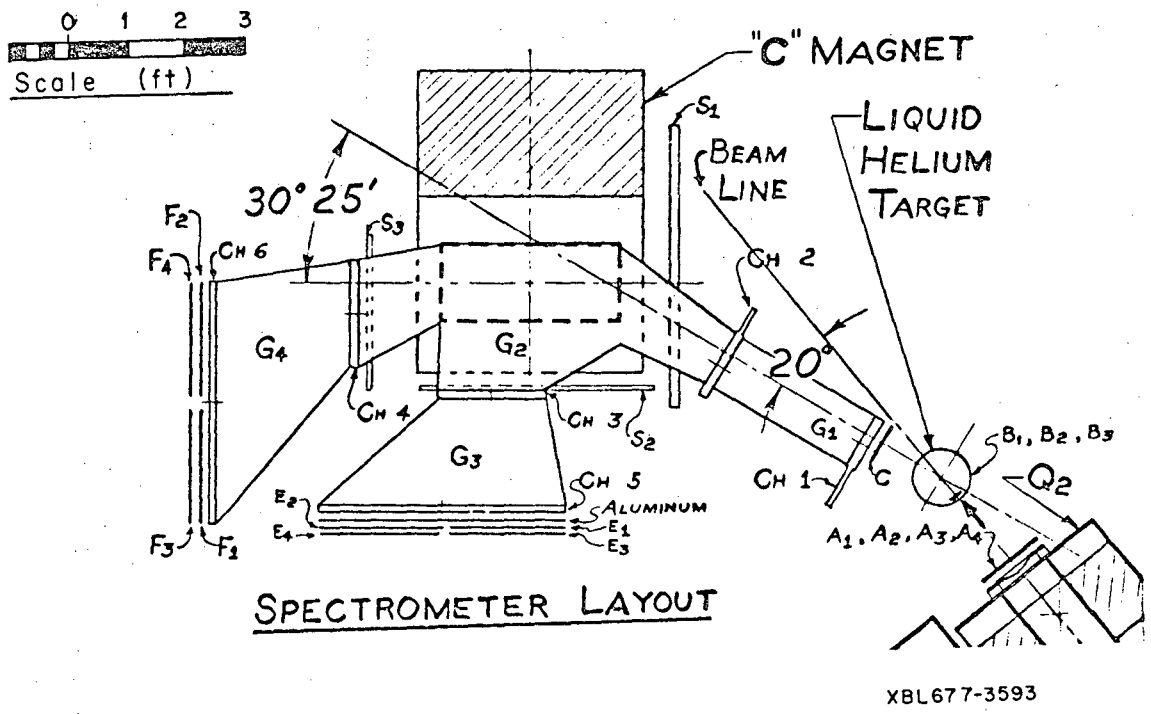

Fig. 7. Spectrometer layout.

"fiducial" distance. Data on chamber construction, running parameters, and performance is given in Appendix A. Suffice it to say here that track-location accuracy in these chambers is better than $\pm$ 0.35 mm.[40] Counter C was 1/32-in. thick by 4-in. wide by 2 5/8-in. high on the side farthest from the pion beam line and 2 3/8-in. high on the side closest to it. The E and F counters were 25 by 18 by 1/4 in. All photomultiplier tubes used were RCA 6810A, selected for high gain and low noise.

The relative positions of chambers and target had been first calculated by assuming a uniform magnetic field and determined finally by the suspended-wire technique. The field was mapped[41] both in the median plane and on planes $\pm$2.5-in. high. The cyclotron field was measured, and its effect on momentum measurements was found to be negligible. Results of the wire orbits were compared with predicted orbits based on the field configuration, and agreement of the order of 1% was found. This is remarkable, considering that the wire orbits were not intended as a fine check on the field, because it was mapped to 0.1% accuracy, the integration routines used were known to yield results better than 0.1%, and wire-orbiting methods allow 1% accuracy at best.

Helium gas bags (G_1, G_2, G_3, and G_4) connected the chambers to minimize particle scattering.

2. Particle Discrimination

Low-momentum protons and deuterons and all pions went through the "E" side of the spectrometer. The heavy particles were eliminated by an aluminum slab between Chamber 5 and the E counters. This acted as a filter, completely stopping the protons or deuterons, and having practically no effect on the pions.

The heavy particles in the momentum range of interest went through

the F side of the setup and were discriminated by TOF measurements, as described in Sec. III. A.9.

F. Electronics

1. Logic Requirements

For Chambers 1, 2, 3, and 5 to be fired, the logic requirement was $[(A_1 \text{ or } A_2 \text{ or } A_3 \text{ or } A_4) \cdot (B_1 \text{ or } B_2 \text{ or } B_3) \cdot (C)] \cdot [(E_1 \text{ or } E_2) \cdot (E_3 \text{ or } E_4)]$; similarly, for Chambers 1, 2, 4, and 6 to fire we required $[(A_1 \text{ or } A_2 \text{ or } A_3 \text{ or } A_4) \cdot (B_1 \text{ or } B_2 \text{ or } B_3) \cdot (C)] \cdot [(F_1 \text{ or } F_2) \cdot (F_3 \text{ or } F_4)]$ (see Fig. 8).

This was achieved as follows: Pulses from the "picket fence" set of A counters were mixed, as were the ones from the "fence" B. Each counter was individually synchronized with the C counter by using the incoming pion beam, and a triple coincidence $(A \cdot B \cdot C)$ with a 12-nsec width was achieved. The pulses of the E(F) counters were properly timed and E_1 and E_2 (F_1 and F_2) were mixed and set in coincidence with the mixed signal from E_3 and E_4 (F_3 and F_4). The coincidence here was narrow (12 nsec), and the resultant signal was finally set in coincidence with the (ABC) signals. Window widths of 25 nsec for the ABCE coincidences and of 32 nsec for ABCF coincidences were set to allow for the different times of travel of the particles. Before timing was done, the voltage on each counter's photomultiplier had been set by "plateauing" its output.

An ABCE signal would inhibit an ABCF trigger, and vice versa. The resolution time for this to occur was about 15 nsec, and only about five discrepancies would be seen in about 15 000 triggers. A master gate operated by the cyclotron spill signal caused the electronics to be operative only after the leading "spike" of the spill was over. This reduced accidental triggers. Furthermore, if an ABCE (ABCF) coincidence occurred, the system was inhibited for the rest of that particular spill.

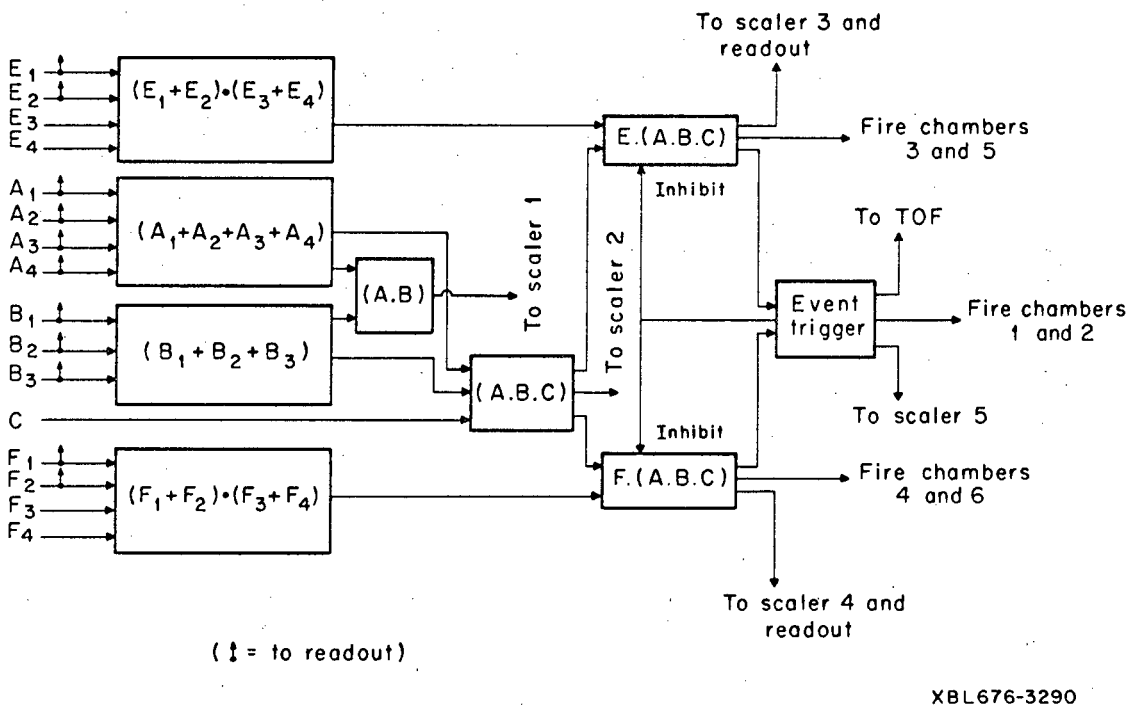

Figure 8. Simplified logic diagram.

2. Logic Acquisition

The signals from each of the A and B counters, and from E_1, E_2, F_1, and F_2 were stored on 80-nsec delay lines. When an ABCE (ABCF) coincidence occurred, gates would open that would allow the signals on these delay lines to set the proper flip-flops. The information in the flip-flops was stored on tape, together with the event number, TOF information, ABCE or ABCF flag, and data from the chambers (see Fig. 9).

The TOF data was used to calculate the masses of the particles from knowledge of the momentum and distance travelled (these two parameters were very accurately calculated by the computer). Given that we were seeking to separate particles whose masses went as M_p, ~ $2M_p$, ~ $3M_p$, no great accuracy in the resolution was necessary for the energy range we worked in.

All signals from the magnetostrictive lines were differentiated, zero-crossed, and then timed by 20-Mc scalers (see Fig. 10, A and B). The differentiation and zero-crossing allowed the clocks to fire and stop on the "center of gravity" of each signal.[42] (Details on the processing of the data from the chambers is given in Appendix B.)

All fast logic was composed of standard modules built by Chronetics, and the data-acquisition equipment was built at this Laboratory.

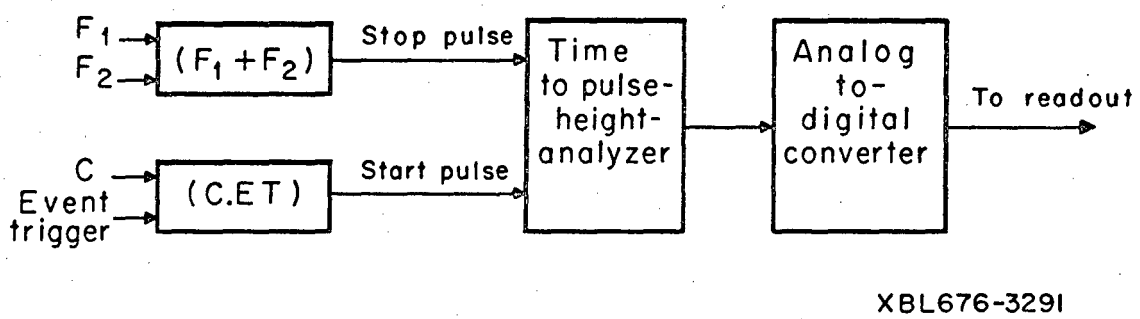

Figure 9. Simplified logic for time of flight measurement.

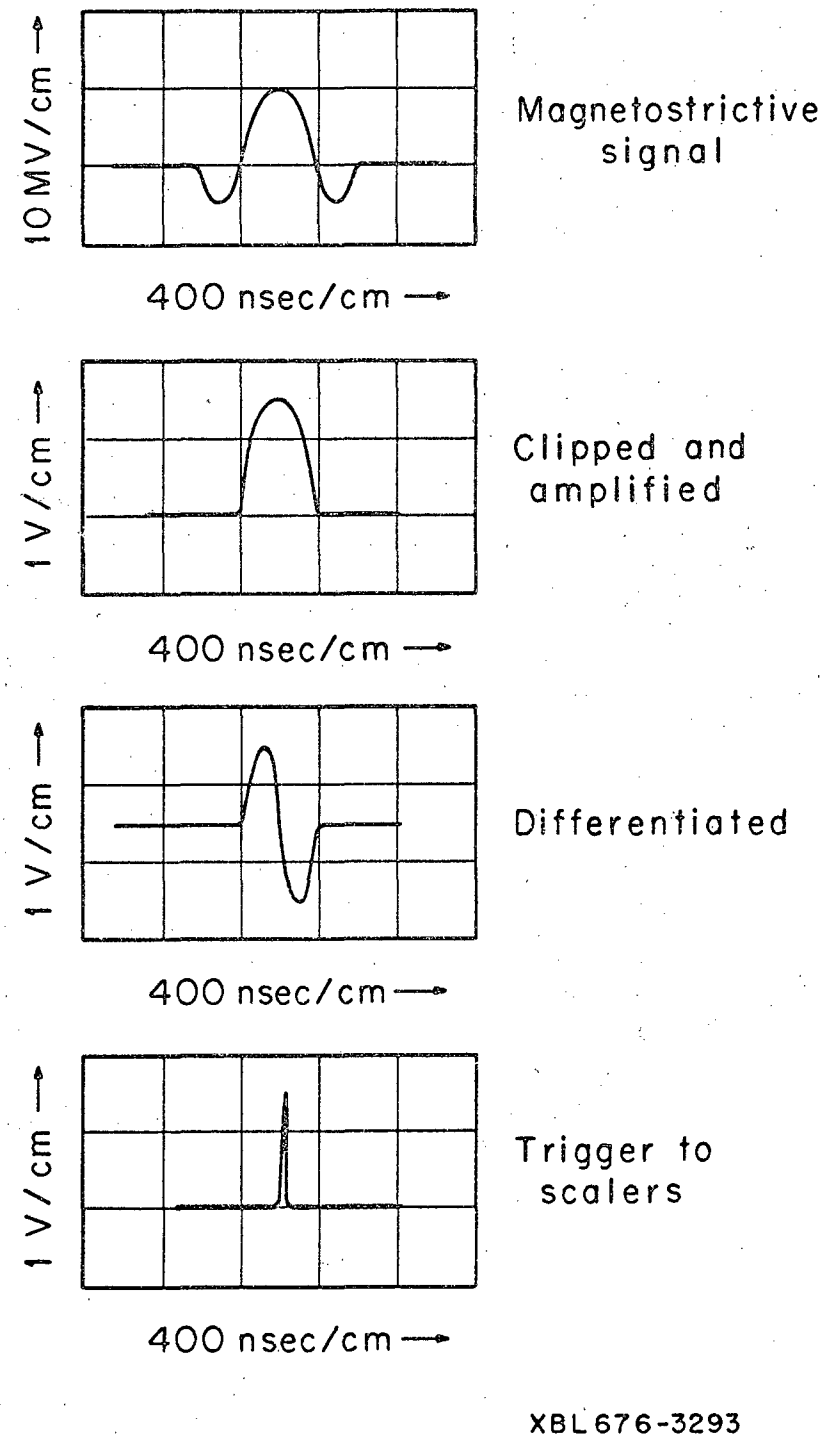

Fig. 10A. Pulse shapes for magnetostrictive signal processing.

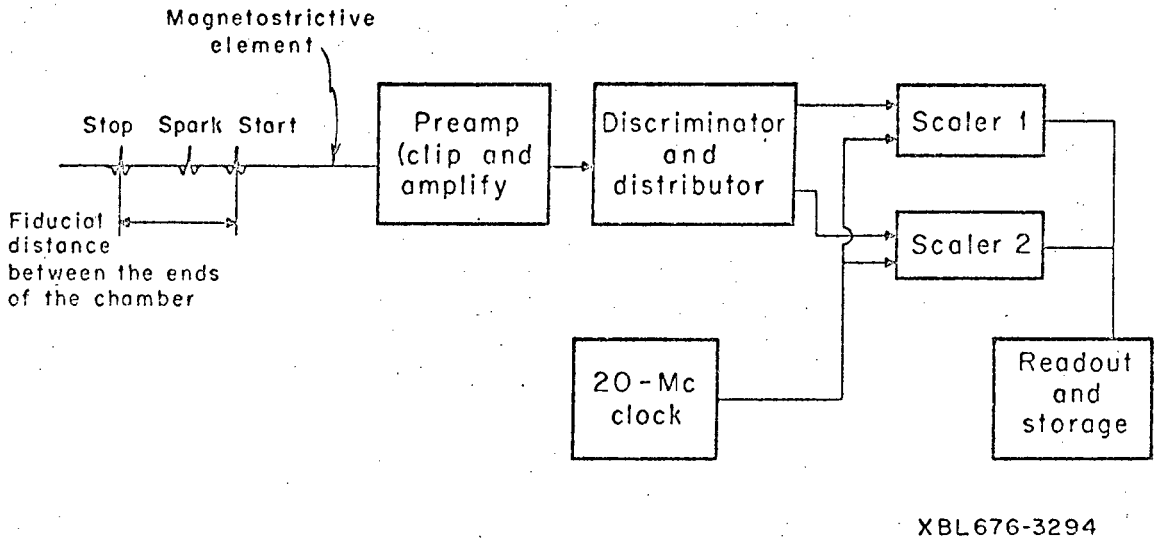

Figure 10B. Simplified logic for magnetostrictive signal processing.

G. Running Conditions

Two spectrometer modes were used for running: (a) π^-, where only ABCE coincidences were accepted, and data on π^--He elastic and inelastic scattering was taken; and (b) π^+, where both ABCE and ABCF coincidences were accepted, and both the π^+ spectra and protons and deuterons were observed.

Runs were effected for each spectrometer mode both with the target full and empty, to obtain the background cross sections from the target assembly.

Other than the data that went onto tape (see Sec. F), we kept a record of the readings of the AB coincidences (beam monitor), ABC, ABCE and (or) ABCF counts for each tape.

It is worth noticing that both chambers 3 and 4 were in the region of the magnet's stray field. While Chamber 4 was only used when the polarity was π^+, Chamber 3 was run under both π^+ and π^- polarities. Given that the polarity of the magnetostrictive signal is dependent upon the external field strength[43] and direction, the signals from two of the magnetostrictive lines were inverted when the field was switched. We kept then two sets of lines to be used as appropriate.

III. DATA ANALYSIS

A. General Analysis

1. Determination of Fiducial Distances

A short program was created to plot histograms of the "tail end" of the counts produced by each one of the wands (see Appendix A). The purpose of this was to determine the value of the fiducial counts for each run.

A wand left to itself will measure a constant (± 0.5 counts) time difference between fiducials. This was manifested by the behavior of the horizontal wand in chamber 3. Due to the way this chamber was located that particular wand was quite inaccessible. From the very first day we installed the chamber through the last run, that delay line yielded a fiducial distance of $2090\ ^{+1}_{-0}$ counts in the π^- mode, and $2100\ ^{+1}_{-0}$ counts in the π^+ mode.

On the other hand, some wands were periodically pulled to clean them, or to change the magnetostrictive line, and for this reason the program was necessary to keep track of the changes produced by these operations.

These data were put onto cards and fed as input into the main program.

2. Finding the Spark Coordinates

The main program found "points" along the magnetostrictive lines as follows: It kept a running average f of the fiducial distance by weighing the new and old data in the following way: $f = (5\ f_{old} + f_{new})/6$. If the fiducial was missing (as was the case in two-spark events; see Appendix B), it supplied the latest f found.

We note that a count was accepted as a fiducial for $f_{new} \leq f_{old} \pm 5$

counts. A typical set of values for f is shown in Table I.

Table I. Comparison of fiducial counts.

Input fiducial counts (Ch. 5)					
2490.0	2468.0	1704.0	1710.0	2682.0	2580.0
Averaged fiducials after 14 569 triggers					
2490.22	2468.38	1704.86	1710.33	2681.60	2580.59

The coordinate x of the spark(s) in a particular wand was then computed from $x = cd/f$, where c is the counts in the line, f is the fiducial count as described before, and d is the distance between fiducials.

3. Determination of a Point

The next step was to superimpose the four wire planes of each chamber together, and all combinations of coordinates were computed. By a generalized least-squares routine we calculated the "center of gravity" of the intersection of any four coordinates (no two belonging to the same plane, of course) and ΔR, the distance from that point to each wire, was computed too. An intersection was accepted as a "4-wire fit" if $\Delta R_{max} \leq C$, where C was a cutoff equal to 0.3 in. for the small chambers (where the particle tracks were almost perpendicular to them) and equal to 1 in. for the large chambers (where the tracks were at large angles). If more than one set of four wires had $\Delta R_{max} \leq C$, then the one with the smallest ΔR was chosen.

Once a 4-wire fit was accepted, the coordinates that produced the fit were eliminated, and the program looked for another one. If none was possible, it tried for 3-wire combinations, following the criteria set

above. If any wires were left over it produced 2-wire fits. This was necessary when more than two sparks had occurred in the chamber.

4. A Line is Born

We realize that the process described above does not take full advantage of all the data the chambers can yield, i.e. each plane is separated by about 1 cm from its neighbor, and this must be taken into account if the accuracy of the data produced by the magnetostrictive lines is to be used fully.

All combinations of points between chambers 1 and 2 (or 3 and 5, or 4 and 6) were fit by lines. These lines were located by a least-squares fit to each of the wires in the set that determined the point. Such lines were named "best-line," and measurements of ΔR on the wire plane are shown in Appendix A.

5. Target Check

Given that only events generated within the liquid He were of interest, we accepted only tracks originating from it. To do this the program computed the scattering point as follows: The data from the A and B counters determined the vertical plane that contained the incoming pion's path. The intersection of this plane with the (accurately known) best-line produced by Chambers 1 and 2 yielded the desired point.

There was an uncertainty in its location of ± 0.35 cm at the front of the target and ± 0.50 cm at the back. This was introduced by the finite widths of the A and B counters.

6. Matching the Lines

Once one or more input lines (IL) were determined, we checked to see if they could be matched with some output line (OL) as determined by chambers 3 and 5 (or 4 and 6). To do this, we had previously computed a

large set of orbits originating at the target and in the momenta ranges of interest. From these orbits two polynomial functions were computed and stored in the main program. One yielded a rough estimate ($\sim\pm 5\%$) of the momentum p as a function of IL and a point x_1 in chamber 3 (or 4). A second function then estimated what coordinate value x_2^1 to expect in chamber 5 (or 6) as a function of p, IL, and x_1.

If there was a point x_2 in the back chambers that was no more than 2-in. away from x_2^1, a match was considered to be found. We had to allow for this large margin in $|x_2^1 - x_2|$ because of the approximate nature of this estimate. The matching was performed purely in the horizontal plane.

7. Calculation of the Momentum

Once an approximate value of the momentum was available (estimated as a function of x_1), an integration was performed by using the estimated momentum $p(x_1)$, and a new coordinate ${}^1x_1$ was computed for this orbit. A new momentum $p({}^1x_1)$ was then estimated. It can be shown[44] that in general $q_{i+1} = p(x_1) - [p({}^ix_1) - q_i]$, where the p(x) stand for estimated momenta, and the q_i for momenta found through iteration. For just one iteration this reduces to

$$q_1 = p(x_1) - [p({}^1x_1) - p(x_1)] = 2\,p(x_1) - p({}^1x_1).$$

As will be mentioned in the next section, a second integration and iteration were performed, and we found that the two values q_1 and q_2 differed by less than 0.1%; q_2 was our selected value for the event's momentum.

8. Event-Acceptance Criteria

As we recall, our data overdetermines the problem, for we measured four points, although only three are needed to compute the momentum

uniquely. Then we could distinguish a good event from an accidental by checking to see if the exit line (computed) matches the one determined by the third and fourth points.

The second integration mentioned served two purposes. The main one was to obtain for the final momentum, the exit track's θ' (angle in the horizontal plane) and ϕ' (angle in the vertical plane). These quantities were compared with θ and ϕ as measured from the OL.

We found that $\Delta\theta = (\theta' - \theta)$ was centered about -0.75 deg and had a HWHM of ± 0.5 deg. Events falling in the $-1.5 \text{ deg} \leq \Delta\theta \leq 0$ deg band were accepted (Fig. 11).

The difference in the vertical angle $\Delta\phi$ was centered about 0.25 deg and had a HWHM of ± 0.8 deg; only the events within the band determined by $-2 \text{ deg} \leq \Delta\phi \leq 1.5$ deg were accepted.

We feel that some comment is necessary on this displacement of the observed distribution of $\Delta\phi$ and $\Delta\theta$ (Fig. 12). The origin of this could be found in a small error in the placing of one of the entrance chambers. For example, a 0.013-in. elevation discrepancy in any one of the chambers could account for the 4-mrad displacement of $\Delta\phi$. As for the $\Delta\theta$ displacement, just a 1/32-in. error in the placing of the rig used to map the spectrometer's field would account for it. Furthermore, $\Delta\phi$ does not affect our momentum calculation, and such a $\Delta\theta$ displacement affects the momentum in the second decimal place only.

If two events in a particular record met these two criteria for $\Delta\theta$ and $\Delta\phi$ (less than 5 in 15 000 triggers), then the one with its value of $\Delta\theta$ closest to -0.75 deg was accepted.

As we saw in Sec. 7, another purpose served by this second integration was to check the value of the final momentum, which as we saw

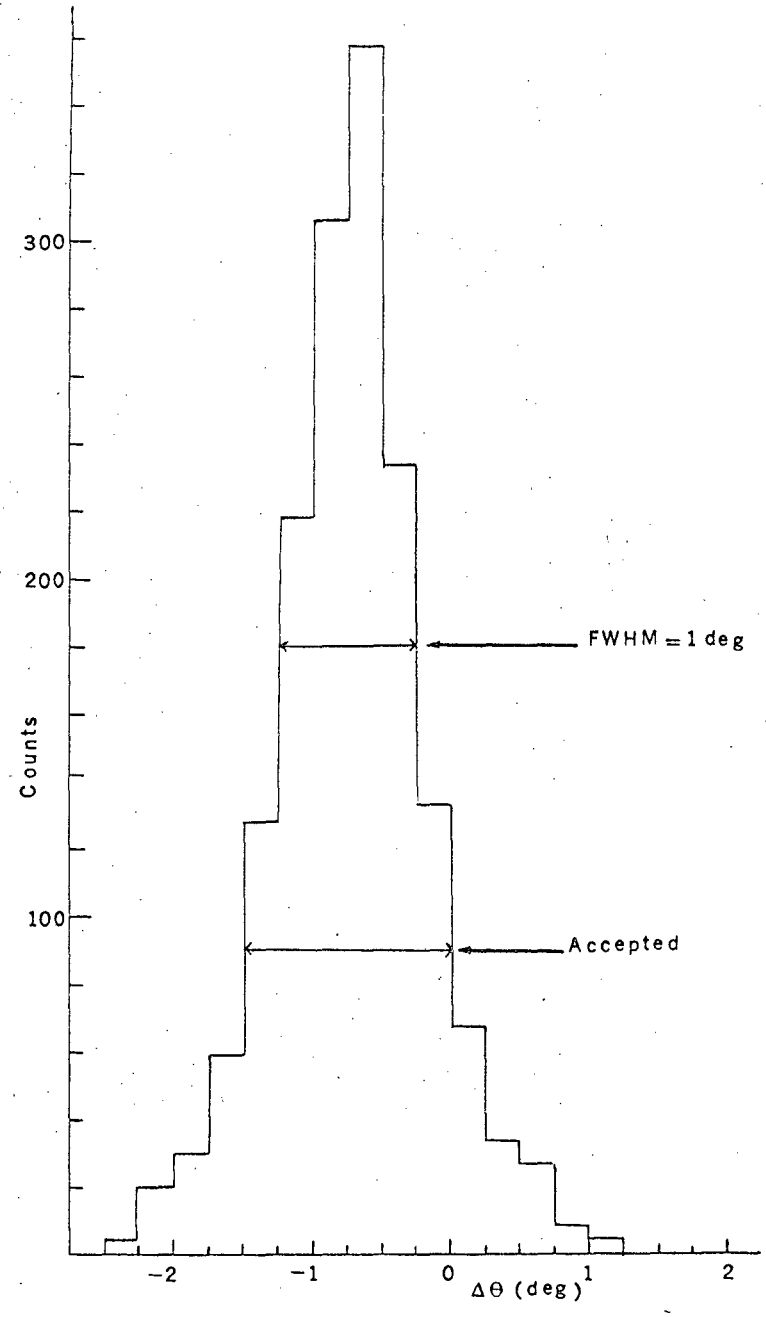

XBL 678-4400

Fig. 11. Distribution of $\Delta\theta$.

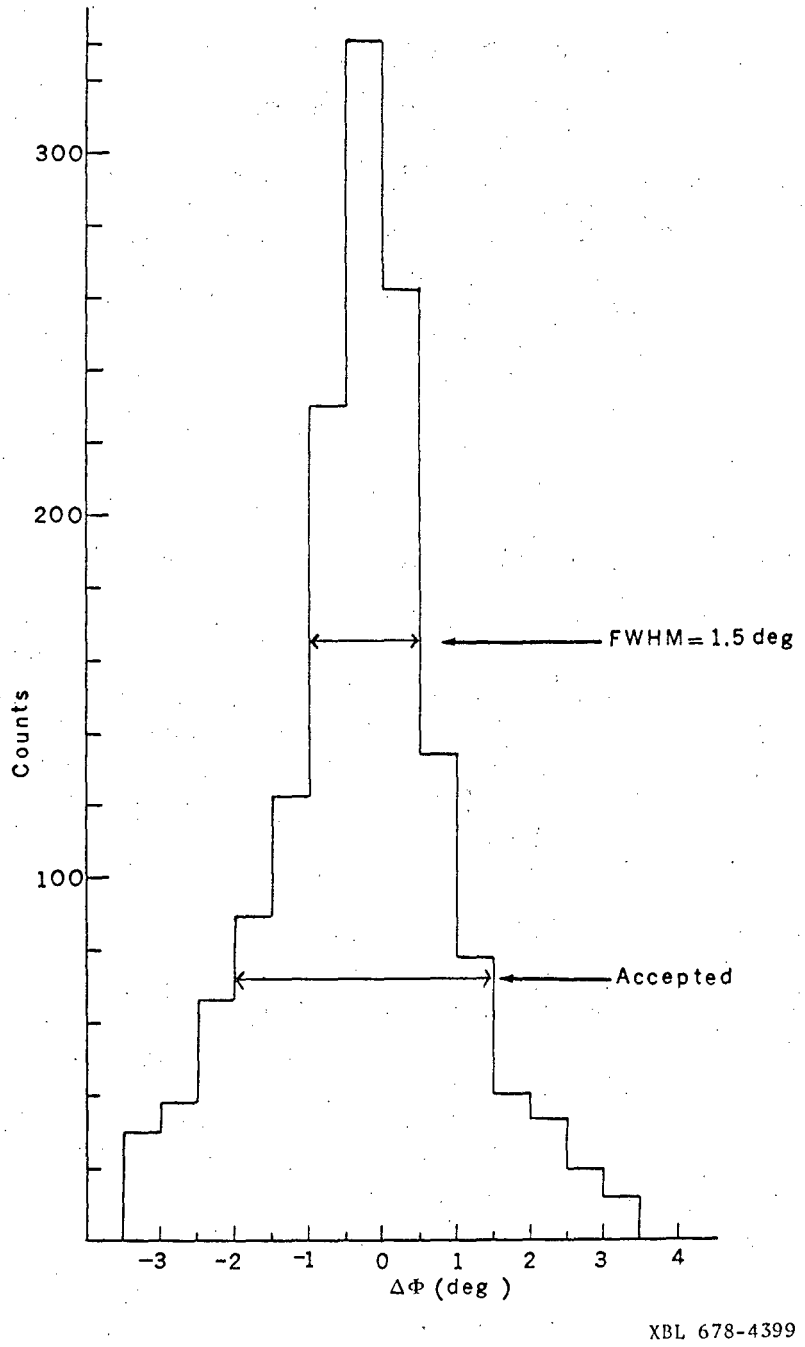

Fig. 12. Distribution of $\Delta\phi$.

in the previous section was arrived at by an iteration. Agreement between the first and second iterations was better than 0.1%.

9. Corrections to the Data

Once and event's momentum was obtained, it was weighted by a previously calculated factor to compensate for the acceptance of the spectrometer (Figs. 13 and 14). Furthermore, in the case of pions (E events), another weighting factor was included to account for π decay in flight. This was of the form e^{t}/τ_{π}, where $t = d*M/p*c$. Here d is the distance (in meters) calculated for the particle's path, M and p are the mass and momentum in MeV and MeV/c respectively, and c is the speed of light in m/sec. For elastically scattered pions this factor is typically 1.25.

For F events, protons and deuterons were separated by the following process: Time-of-flight information yielded the time, t, for the particle to go from the C to the F counters. Given that the momentum p in MeV/c was well known, the mass M in MeV of the particles was found from

$$M = (p/\beta)(1 - \beta^2)^{1/2},$$

where $\beta = d/tc$. From a comparison of M with the mass of the proton and deuteron, we found which kind of particles we were dealing with (Fig. 15).

The computed momenta were corrected then for energy loss in the components of the spectrometer, including target walls, by use of functions as given in Fig. 16. Then, the amount of liquid He the scattered particle had traversed was computed. A further correction was applied to compensate for energy loss in the He as shown in Fig. 17. Finally a transformation to the c.m. was performed, taking care of accounting for the energy loss (of the incoming pion) in the target.

The angle between the incoming and outgoing particles was measured between the vertical plane of the former and the exit line of the latter.

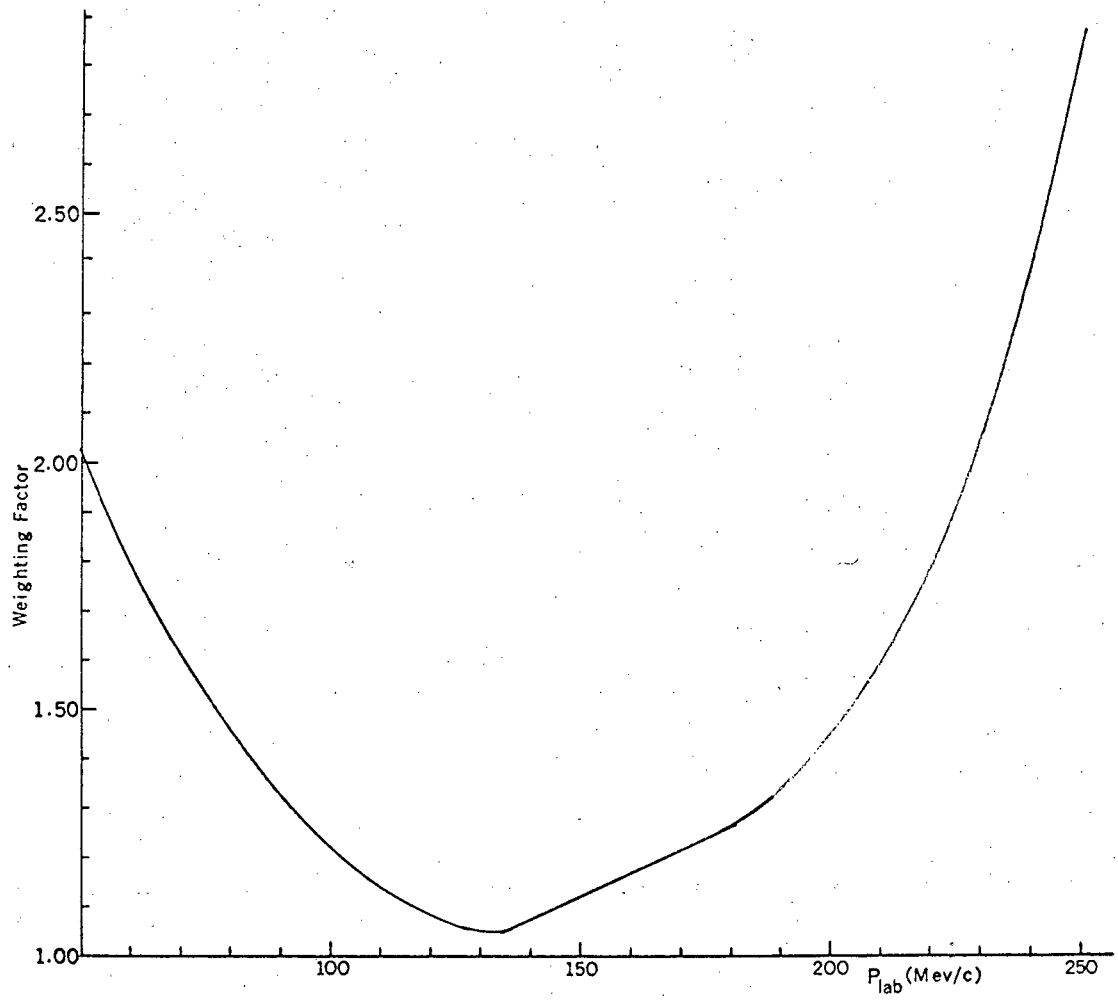

XBL 678-4398

Fig. 13. Weighting factor vs. computed momentum. The weighting factor is a correction for magnet acceptance at the low-momentum end of the spectrometer.

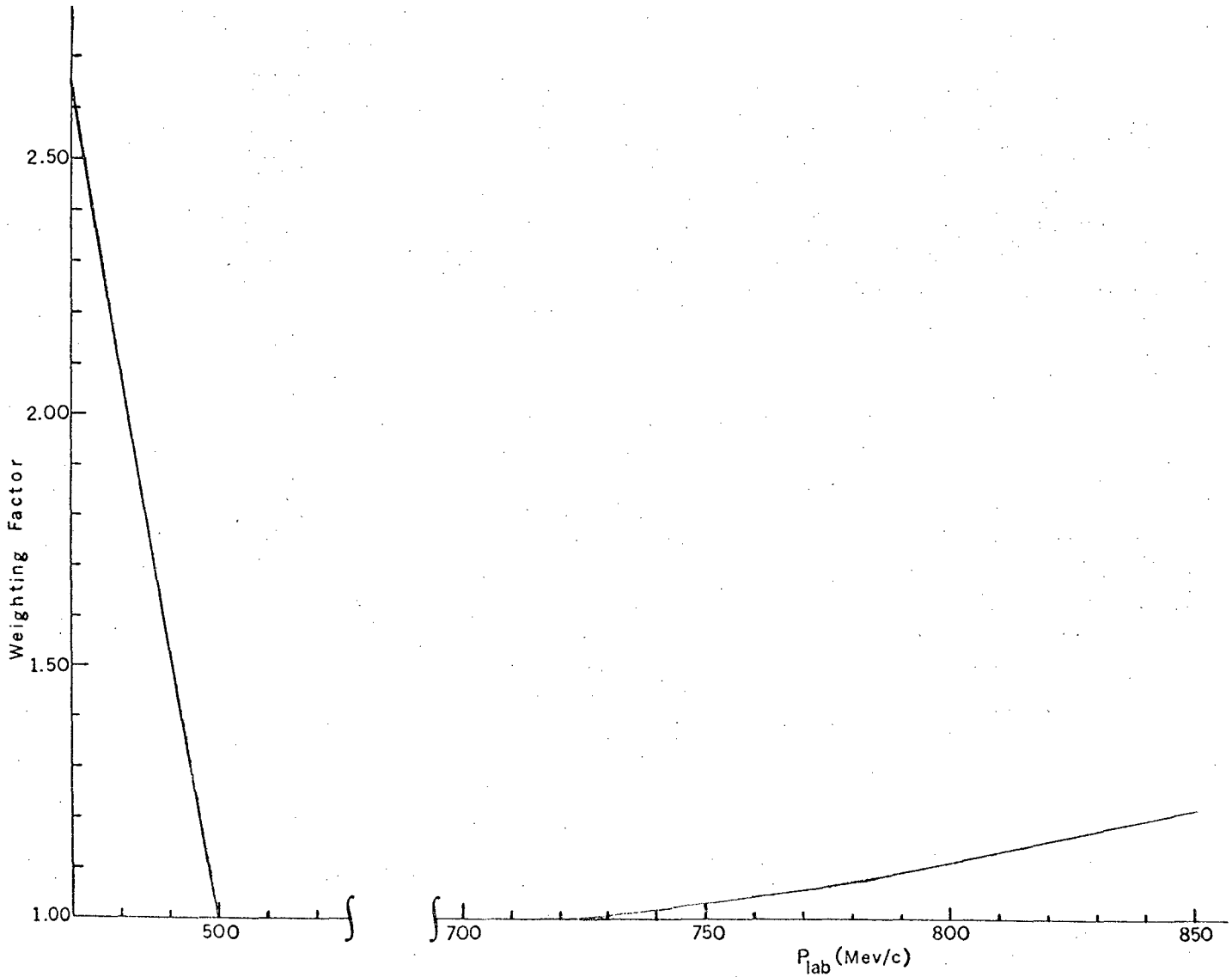

XBL 678-4397

Fig. 14. Weighting factor vs. computed momentum. The weighting factor is a correction for magnet acceptance at the high-momentum end of the spectrometer.

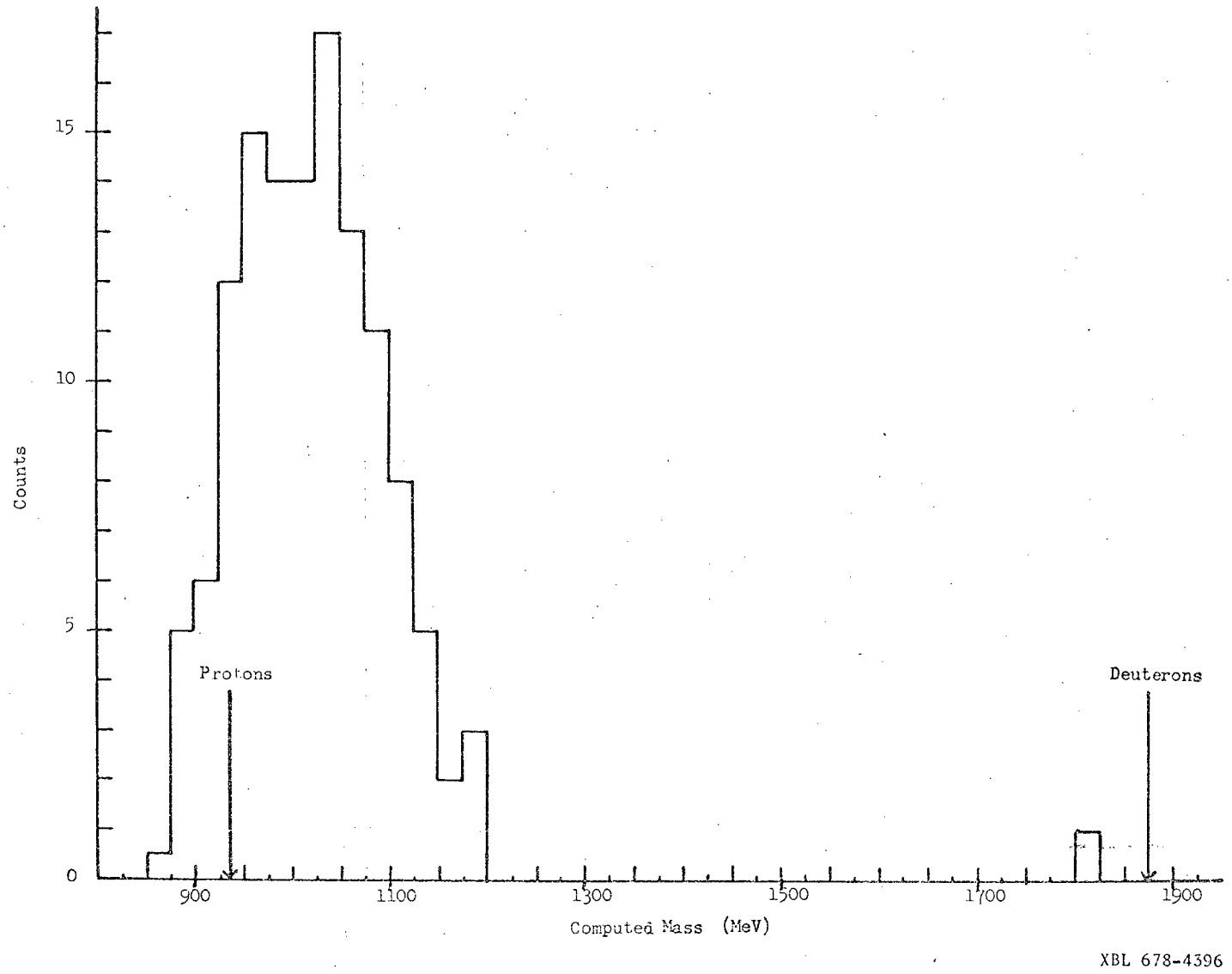

Fig. 15. Typical mass spectrogram, for 127 events.

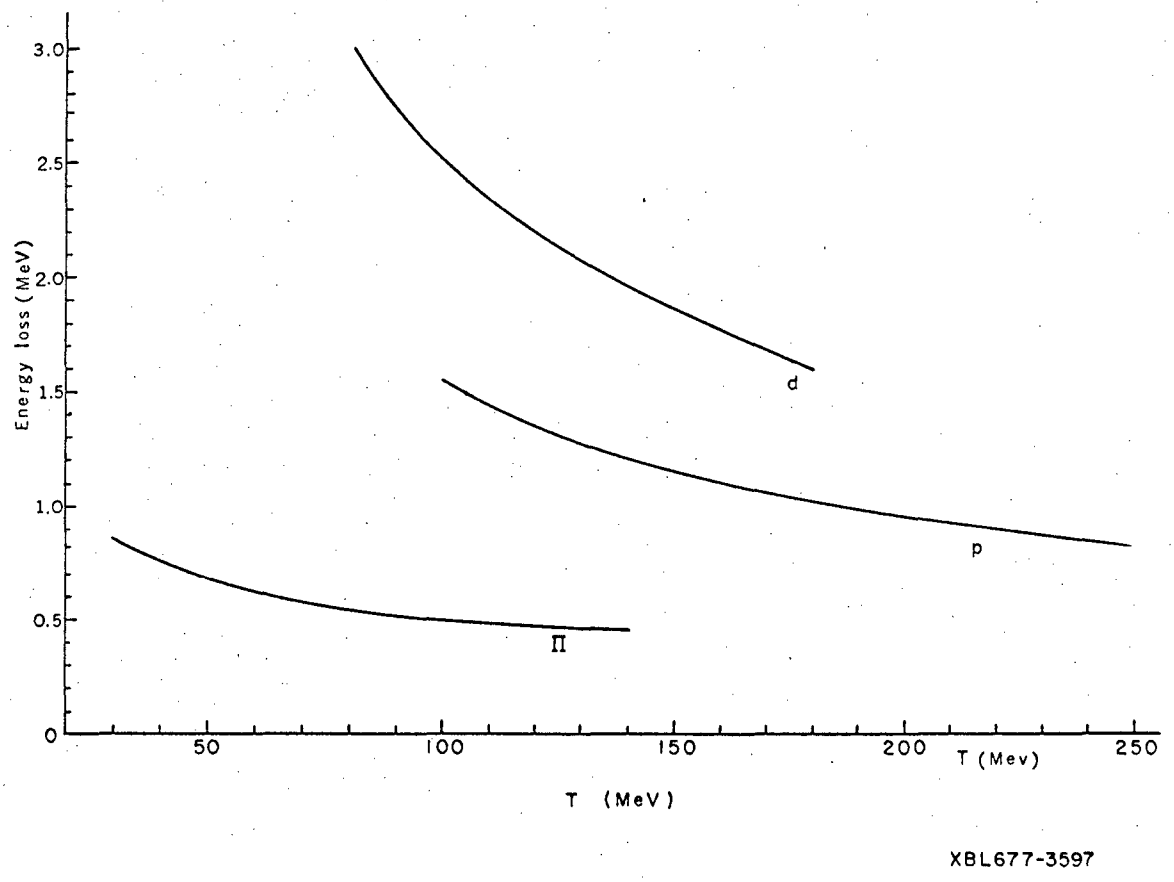

Fig. 16. Energy loss in the spectrometer vs. kinetic energy for deuterons, protons, and pions. The liquid-He contribution is not included.

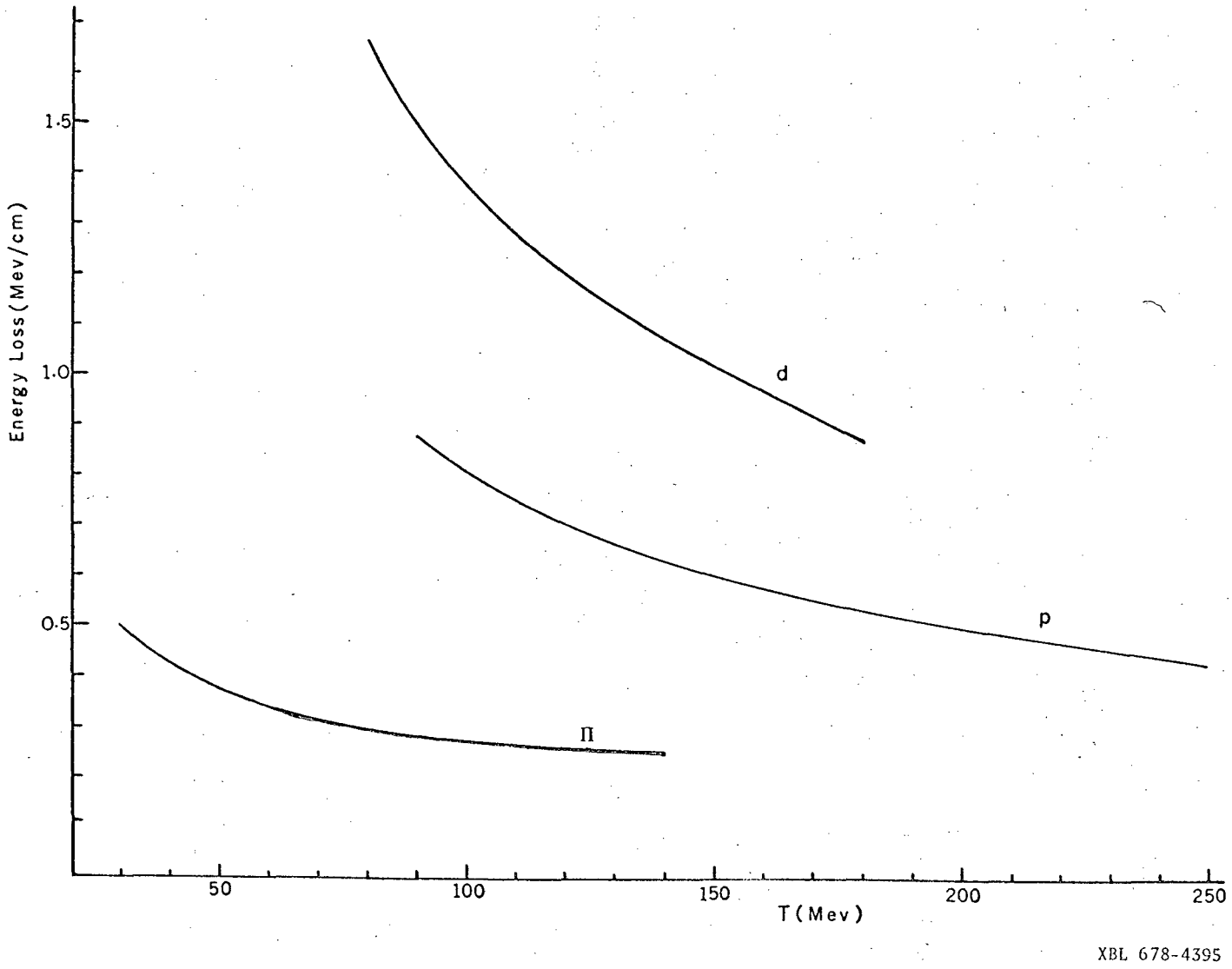

Fig. 17. Kinetic energy vs. energy loss of deuterons, protons, and pions in 1 cm of liquid He.

This was done at the same time that the intersection point in the target was found (see Sec. 5).

10. The Last Step

The last step consisted of a routine that histogrammed the properly weighted and corrected c.m. energy for pions, protons, and deuterons; it showed too a top and side view of the target indicating the number of events within 1/2-cm. cubes. A punched card was produced for each event; such a card and the information in it are shown in Fig. 18.

The steps described in items 2 through 10 were all performed in one program.

118.01 540.16 1.000 -.95 3.18 -1.22 962 1100 011 F -.81 -.21 134 1

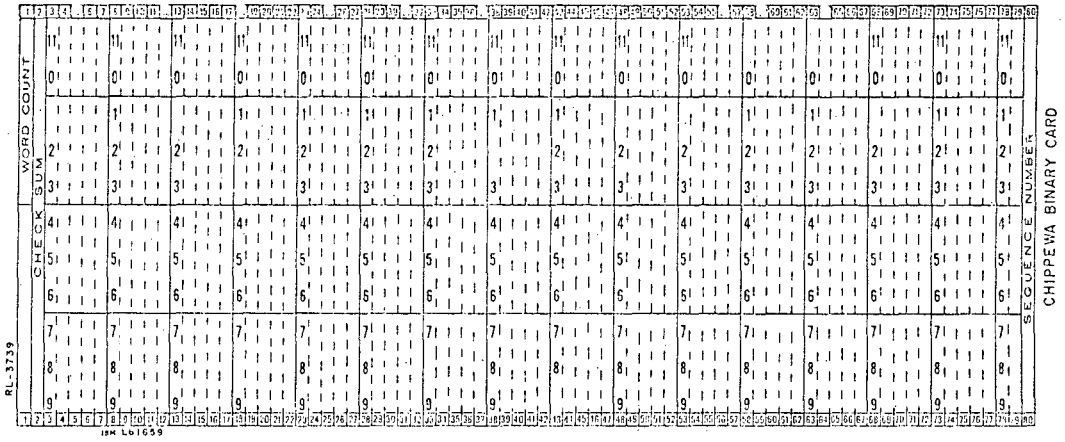

Fig.18. Event Card.

Column range: 2-7 : Center of Mass Energy (corrected).
9-14 : Laboratory Momentum
17-21 : Event Weighting Factor
23-27 : X
29-33 : Y } Target Coordinates
35-39 : Z
42-45 : Mass
47-50 : A Counters
52-54 : B "
56 : E/F Event Flag
57-61 : $\Delta\Theta$
62-66 : $\Delta\Phi$
68-70 : Tape Number
72 : File "

XBL677-3599

B. Error Estimates

1. Scattering in the Spectrometer

The momentum of a particle was determined uniquely by knowing the coordinates of the input line IL and one exit point, the second exit point serving mainly as a check on the event's validity.

We now calculate the effects that scattering and uncertainties in the determination of the particle coordinates have on the value of the momentum.

The effects of scattering are only important on the horizontal plane, and we will restrict our analysis to that plane.

The quantity we are interested in is the fractional change in the computed momentum dp/p. This is evidently equivalent to computing the fractional change in the radius of curvature $d\rho/\rho$.

The field in the magnet can be approximated very accurately by a uniform field, which will greatly reduce the complexity of our calculations without affecting their generality. Due to the geometry of the set up, we must consider two cases: the first one for the F side, where the wedge angle is 0 deg, as in Fig. 19; and the second one for the E side, where the wedge angle is 90 deg, as in Fig. 20. Defining our quantities as in those figures, we find $d\rho/\rho$ as a function of dy and $d\epsilon_1$. We note that dy arises from two contributions--one at the input side, mainly due to scattering; the other at the output side, due mainly to the uncertainty of the location of the track at Chambers 3 or 4.

We first deal with the case of no wedge angle. It is easy to see that

$$\rho = \frac{\alpha}{2 \sin\left(\frac{\epsilon_1 + \epsilon_2}{2}\right)} ,$$

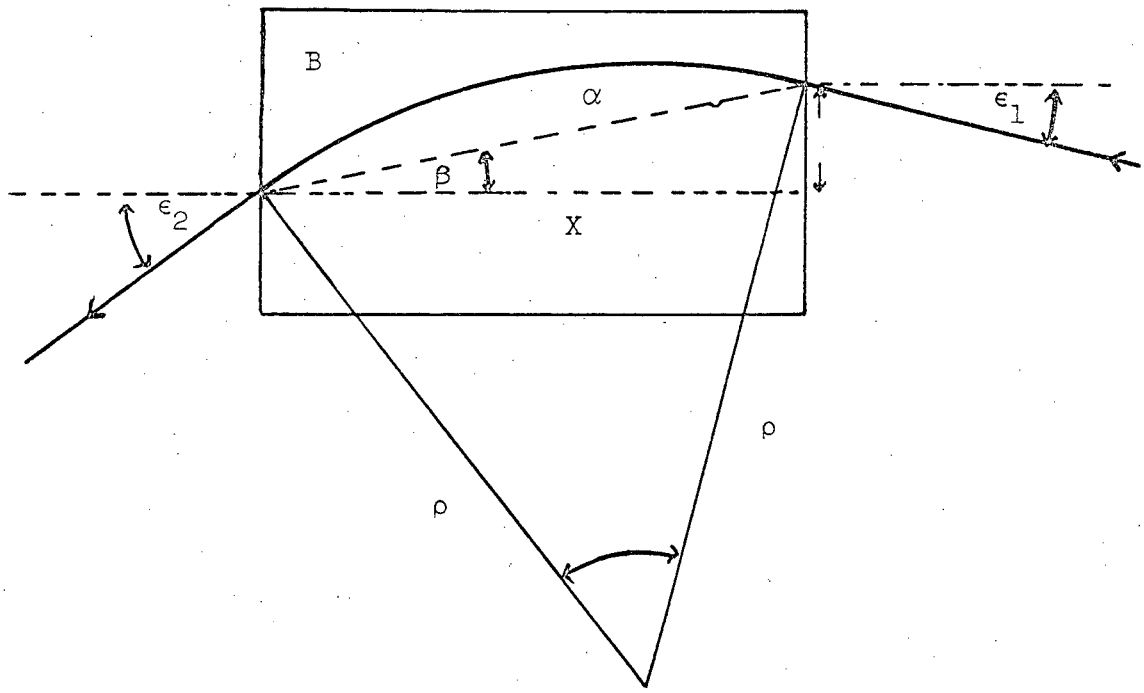

XBL 678-4393

Fig. 19. Simplified spectrometer geometry for proton and deuteron momentum measurements.

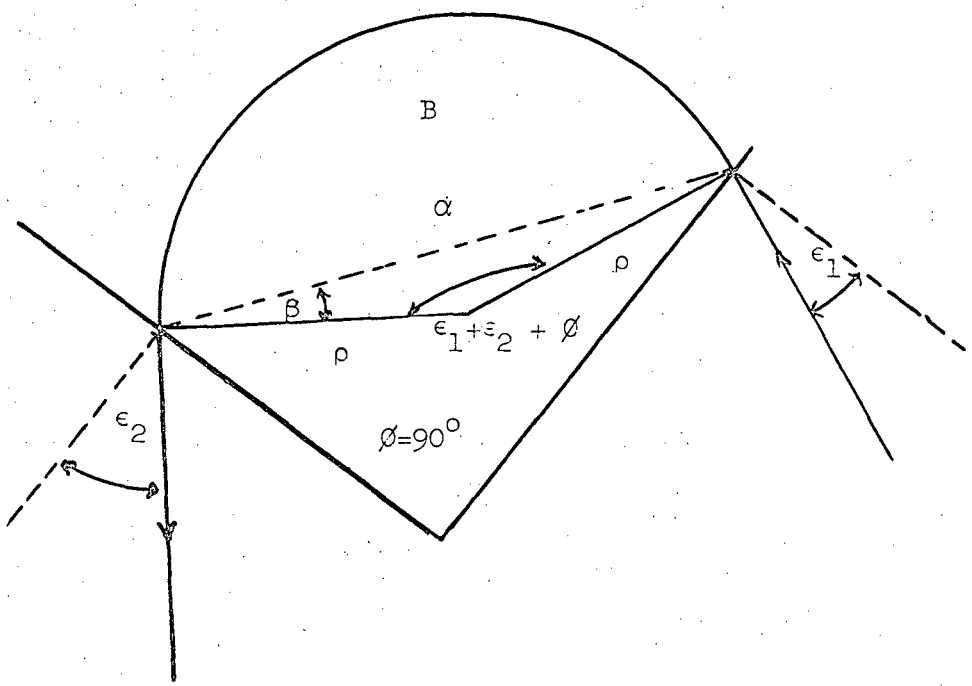

XBL 678-4394

Fig. 20. Simplified spectrometer geometry for pion momentum measurements.

where $\alpha = (x^2 + y^2)^{1/2}$, and x is fixed. Through straightforward differentiation we obtain

$$\frac{dp}{p} = \left| \frac{\sin(\epsilon_2 - \epsilon_1)}{2x} dy \right| + \left| \frac{\cot\left(\frac{\epsilon_1 + \epsilon_2}{2}\right)}{2} d\epsilon_1 \right| .$$

We draw the reader's attention to the fact that ϵ_2 enters here as a fixed parameter, because its value <u>is not used</u> in determining the momentum.

The entrance angles are $\epsilon_1 = 30 \pm 4.5$ deg, and the exit angles vary between 10 and 20 deg, so that 18 deg $\lesssim (\epsilon_1 + \epsilon_2)/2 \lesssim 27$ deg. This leads to $\cot[(\epsilon_1 + \epsilon_2)/2] \lesssim 3$, while $\sin(\epsilon_2 - \epsilon_1)$ is approximately 0.3.

In the rectangular-field approximation, x is about the length of pole tips + 1/2 gap width at each end. For a 36-in. pole tip and 8-in. gap, we have x = 44-in. ≈ 110 cm. Thus we have $\frac{dp}{p} \simeq |1.6 \times 10^{-3}\ dy| + |1.5\ d\epsilon_1|$, where dy is in cm and $d\epsilon$ is in radians. If dy is of the order of 10^{-1} cm, then the first term is certainly less than 10^{-3}, or 0.1%. We will drop any further considerations having to do with it, and we finally write

$$dp/p \lesssim 1.5\ d\epsilon_1 . \qquad (1)$$

In the second case, where the wedge angle is 90 deg, we obtain

$$\rho = \frac{\alpha}{\sqrt{2}\,[1 + \sin(\epsilon_1 + \epsilon_2)]^{1/2}} .$$

From our previous analysis we know that the term in $d\alpha (\propto dy)$ can be neglected; then it is straightforward to arrive at

$$\frac{dp}{p} = \frac{\cos(\epsilon_1 + \epsilon_2)}{2[1 + \sin(\epsilon_1 + \epsilon_2)]}\ d\epsilon_1 .$$

As before, $\epsilon_1 = 30 \pm 4.5$ deg, but the exit angle ϵ_2 varies between - 45 and 0 deg, so that - 20 deg $\lesssim (\epsilon_1 + \epsilon_2) \lesssim 34$ deg. Given that the cosine

term is even, it does not vary much in this range, and the sine term determines that dp/p becomes largest at - 20 deg. Thus we write

$$\frac{dp}{p} \lesssim 0.7\, d\epsilon_1. \qquad (2)$$

Equations 1 and 2 then give the maximum error in the resolution of the spectrometer due to scattering, and the problem has now been reduced to determining upper bounds for $d\epsilon_1$.

A problem arises when considering scattering in the chambers, for they are built of wires, and either a particle hits one or goes through the plane without scattering at all. We have assumed that four wire planes are "many," and we average out these wires, distributing the aluminum uniformly. Thus the four-wire planes in each chamber have an average density of 0.02 g/cm^2. This is, of course, true for chambers 1 through 4, but not for 5 or 6. The back chambers have a higher density, but this did not affect us, as scattering in those chambers is not relevant.

Each input chamber had two 2-mil Mylar windows (5.6×10^{-3} g/cm^2/window).

The effect of the He-Ne mix in the chamber is neglected, and the amount of He gas between them is 1.3×10^{-2} g/cm^2.

Only Coulomb scattering is to be considered, for nuclear scattering is rare, and it generally yields angles large enough that an event due to a particle that underwent such scattering would be eliminated by the cutoffs described in Sec. III. 8.

For our calculations we use

$$\phi_{rms} = \frac{15}{P(\mathrm{MeV}/c)\beta}\,(L/x_o)^{1/2} \text{ and } Y_{rms} = \frac{L\,\phi_{rms}}{\sqrt{3}},$$

where L is the length of material traversed, and x_o is its radiation length.

We define $d\epsilon_1 = |\epsilon_0 - \epsilon_1|$, where ϵ_0 is the angle as determined by the chambers, and ϵ_1 is the angle at which the particle enters the magnetic field. For typical momenta we find

$$d\epsilon_1(\pi) \lesssim 0.9 \times 10^{-2},\ d\epsilon_1(p) \lesssim 1.3 \times 10^{-3},\ \text{and}\ d\epsilon_1(d) \lesssim 4.1 \times 10^{-3},$$

including the effect of uncertainties due to spark location in the chambers. Thus, from combining these quantities with Eqs. (1) and (2) we obtain $dp/p \lesssim 0.6\%$ for pions, $dp/p \lesssim 0.2\%$ for protons, and $dp/p \lesssim 0.6\%$ for deuterons.

2. Determination of the Scattering Angle in the Target

Two sources contributed to an uncertainty in the computation of this angle: the first was due to scattering in the exit path, which produced an uncertainty of about 10^{-2} rad in the angle between best-line and the actual direction of scattering.

The second source was due to the finite width of the A and B picket fences. The A and B counters determined regions 0.75-in. and 0.25-in. wide respectively, and they were separated by 21.25 in. The uncertainty in the angle determined then was $\pm 2.35 \times 10^{-2}$ rad. Thus, the total uncertainty expected was $\Delta\theta \simeq \pm 4.5 \times 10^{-2}$ rad $\approx \pm 2.5$ deg.

To determine how such a spread would affect the relativistic transformation to the c.m. system, we calculated the "gradients" $dp/d\theta$ at 20 deg. Table II shows our results.

Table II. Pion, proton, and deuteron "gradients" at 20 deg.

Particle	$dp/d\theta$ (MeV/c-deg)	p (MeV/c)	dp (MeV/c)	dp/p (%)
π	0.100	241	± 0.25	± 0.1
p	0.465	670	± 1.2	± 0.08
d	0.824	800	± 2.1	± 0.26

3. Determination of the Point of Intersection in the Target

Due to the finite width of the counters, the position of this point was uncertain by as much as 0.5 cm (see Sec. III. A.5). This produced an uncertainty in the c.m. energy of the scattered particle, because the program was not able to compute the correct length of liquid He this particle transversed. The errors introduced in the momentum were from $\pm 0.25\%$ to 1% for deuterons, from $\pm 0.1\%$ to $\pm 0.4\%$ for protons, and from $\pm 0.1\%$ to $\pm 0.9\%$ for pions. We can say that, in general, this was the largest single source of error.

4. Energy Resolution

Accounting for the momentum resolution as estimated in Sec. I [keeping in mind that $dE/E = (p^2/E^2) \times (dp/p)$], and including the uncertainties discussed in Secs. II and III, we find

$$dE(\pi) \lesssim 1.0 \text{ MeV}, \quad dE(p) \lesssim 0.6 \text{ MeV}, \text{ and } dE(d) \lesssim 1.2 \text{ MeV}.$$

IV. RESULTS

A. $\pi^- + He^4$ and $\pi^- + He^{4*}$ Channels

Figure 21 shows the scattered π^- energy spectrum in the c.m. system. Our resolution is determined by the FWHM (~ 1 MeV) of the elastic peak. The interesting feature of this spectrum is the large cross section observed at 32-MeV excitation energy of the α particle. This possible level is narrower than our experimental resolution.

The cross sections given are corrected for (a) μ^- and e^- contamination of the initial beam, (b) solid-angle acceptance of the helium target, (c) spectrometer acceptance, and (d) π decay in flight. The background has been subtracted. It can be seen in Fig. 21c.

B. $\pi^+ + 4n$ Channel

The resultant π^+ spectrum is shown in Fig. 22. Superimposed on it can be seen undisturbed phase space, and the effects of adding the 2n singlet-even interaction between two of the neutrons in one pair, or between the two neutrons in each pair. We find a slightly better fit to the data by using the second possibility. An upper limit of $1.38 \pm 50\% \times 10^{-4}$ μb/sr-MeV is established for the formation of a tetraneutron with a binding energy (B. E.) between -10 and 10 MeV. The experimental resolution was 1 MeV, as above. Corrections were done as in A, and background was negligible.

C. p + 3n Channel

Figures 23 and 24 show the proton energy spectrum in 2- and 5-MeV bins respectively. Superimposed on these we see the distributions to be expected from phase space, and the effect of adding the singlet-even interaction between two of the neutrons in the final state.

Cross sections are corrected for factors (a), (b), and (c) as in A.

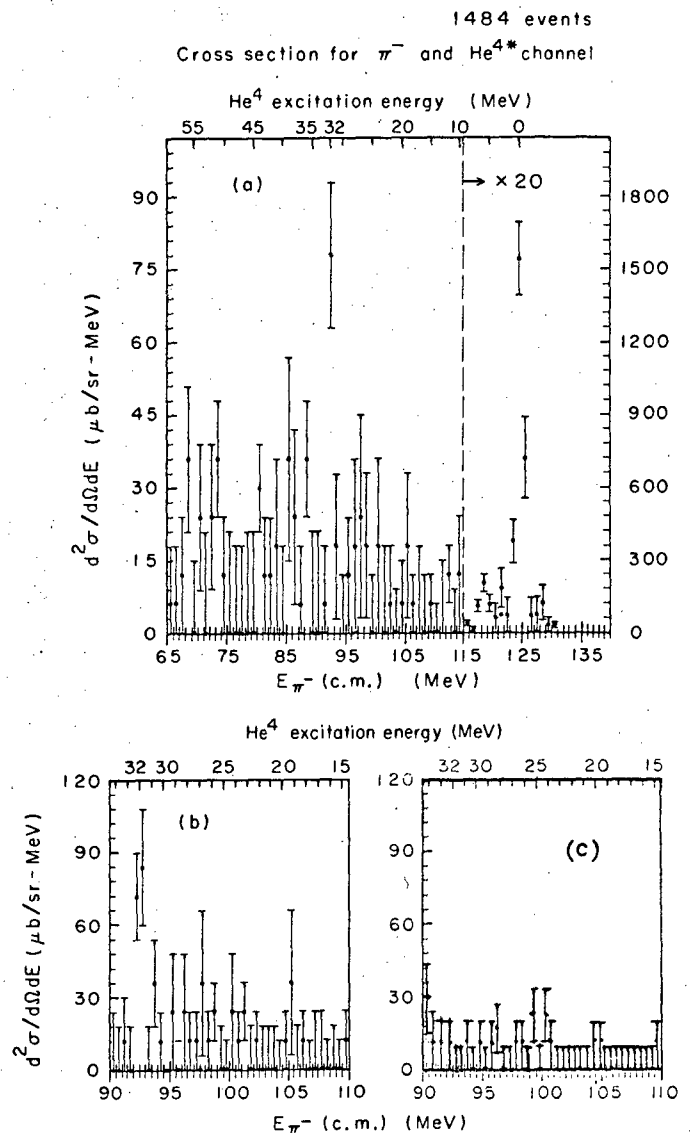

XBL 678-4384

Fig. 21. (a) Full spectrum, inelastic-region spectrum, and background events. Bin width for (a) is 1 MeV; for (b) and (c), 0.5 MeV.

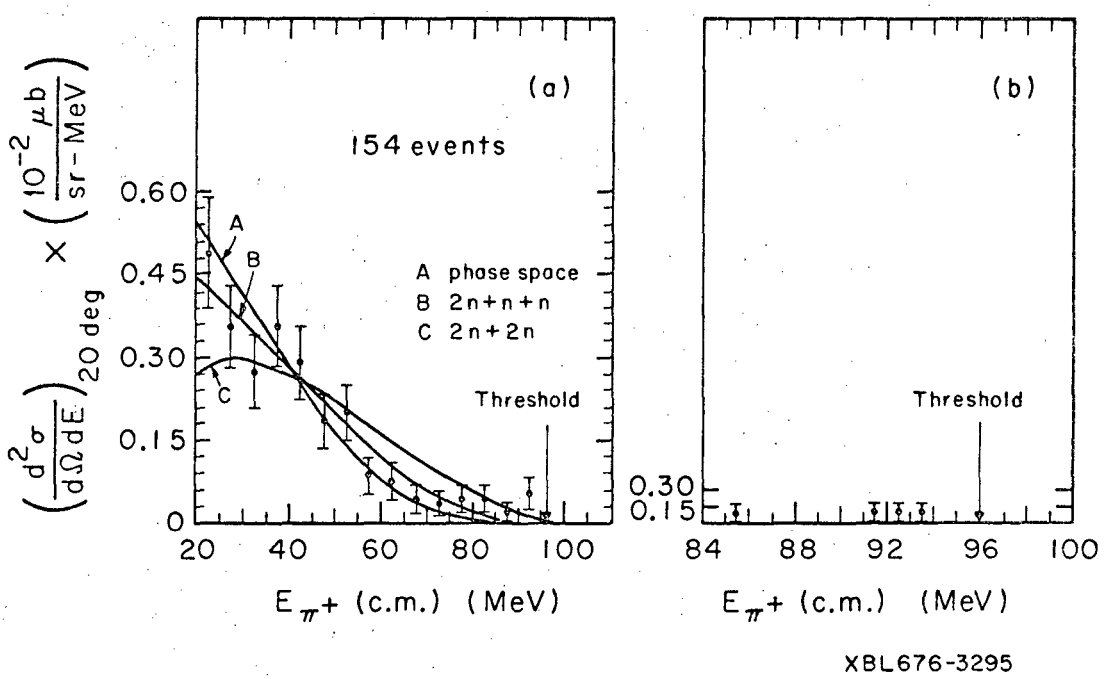

Figure 22. π^+ spectrum.

(a) 5-MeV bins

(b) 1-MeV bins around threshold for n^4 production.

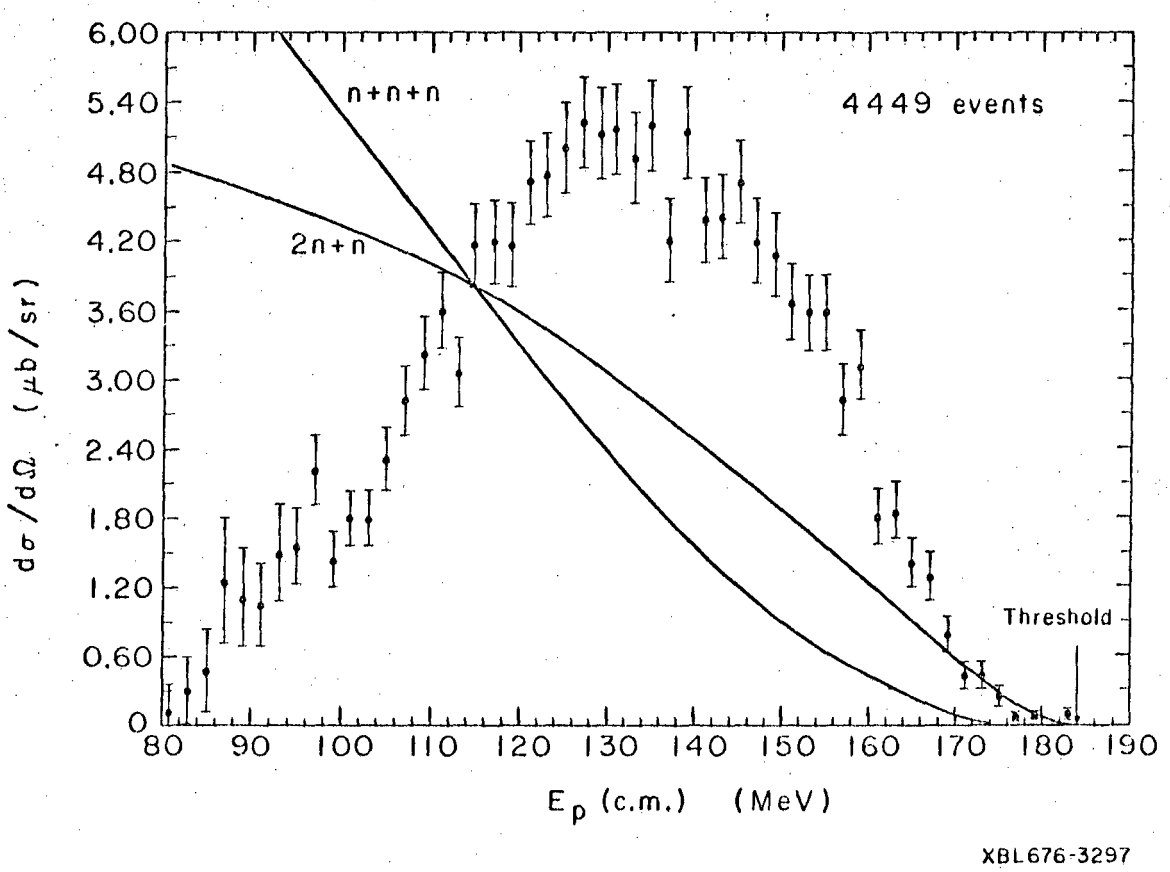

Fig. 23. Proton spectrum, with 2-MeV bins.

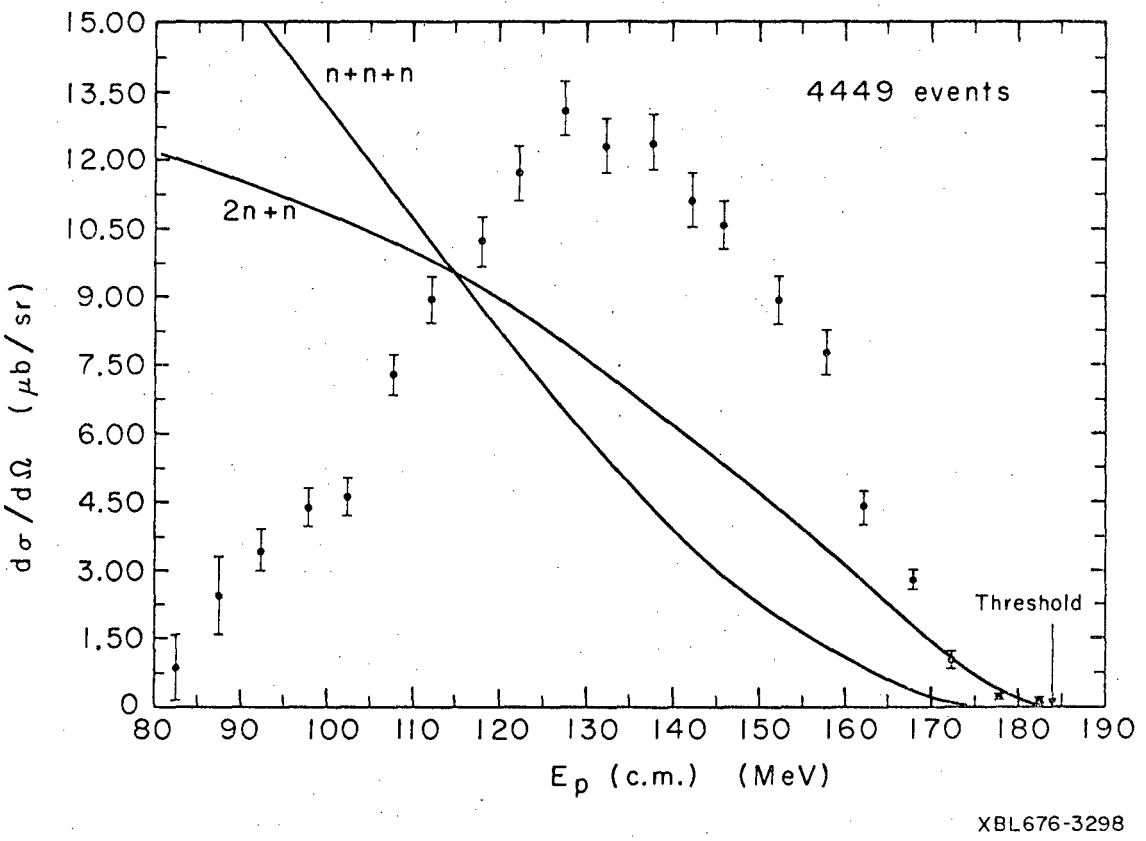

Fig. 24. Proton spectrum, with 5-MeV bins.

The background was negligible. An upper limit of 0.0123 $\pm$0.0025 μb/sr-MeV is established for the cross section for production of a trineutron with -3 MeV < B. E. < 3 MeV. The experimental resolution was ≈ 0.6 MeV.

D. d + 2n Channel

Only four deuterons were seen in the range from 470 MeV/c to threshold at 801 MeV/c in the lab system. This yields the result that

$$\frac{\sigma_{\pi^- + He^4 \to p + 3n}}{\sigma_{\pi^- + He^4 \to d + 2n}} = 1150 \pm 50\%.$$

The integrated cross section for this reaction in the c.m. system is $\sigma = 0.0012 \pm 50\%$ μb/sr-MeV. These cross sections are corrected as in Sec. C. Background was nonexistent here.

V. INTERPRETATION AND CONCLUSIONS

A. $\pi^- + He^{4*}$ Channel

Only one excited level of the α particle was observed. Its energy is at 32 $\pm$1-MeV above the ground state, and it probably corresponds to the 30-MeV level seen by Charpak.[21] There is no discrepancy between our value for the excitation energy and his, for the width of the peak in that experiment was more than 2 MeV, thus overlapping our result. The width of the level as we determined it is less than 1 MeV. Because this was intended as a survey experiment on many channels, we did not attempt a study of the angular behavior of the level, and no J value can be assigned from our data.

Something can be said though about its isospin state. The initial π^--He^4 system has T = 1, and given that $T_{\pi^-} = 1$, the He^{4*} can be left in either of the states T = 0, 1, or 2. The T = 0 state corresponds to a singlet of course, but for T = 1 we would have a triplet H^4 -He^{4*}- Li^4, and for T = 2 we should find a quintuplet, n^4 - H^4 - He^{4*} - Li^4 - p^4. Our negative results in the DCX experiment tend to indicate that n^4 does not exist. This immediately limits the possible T values of the 32-MeV level to 0 or 1.

Something can be said about this second possibility: There is some evidence[15] that H^4 unstable against dissociation exists, even though particle-stable H^4 has not been seen. As we mentioned before, Cohen et al. observed the reactions $Li^6(\pi^-,d)H^4$ and $Li^7(\pi^-,T)H^4$, finding H^4 with $0 < B.E. < 5$ MeV against its breakup into four free nucleons.

There is evidence for the existence of Li^{4*} as reported by Tombrello et al.;[30] furthermore Beniston et al.[31] observe that analysis of the π^- and p momenta in the decay of the He^4_Λ hyperfragment ($He^4_\Lambda \rightarrow \pi^- + p + He^3$)

yields evidence of a Li^4 state with an energy that corresponds to ~ 30 MeV excitation of the α-particle.

We believe that the present data indicate the existence of the I-spin triplet, and that it corresponds to an excited level of He^4 with E = 32 MeV (Fig. 25).

B. d + 2n Channel

The low cross section found for this reaction yields a low probability for the d + n + p and d + d components of the wave function of the α particle. Furthermore, it tends to indicate that the final-state interaction between the proton and one of the neutrons in the p + 3n channel is small.

C. p + 3n Channel

In the reaction studied, the upper limit in the cross section for formation of a trineutron with - 5 MeV < B. E. < 5 MeV is determined to be $7.5 \pm 4.5 \times 10^{-33}$ cm^2/sr-MeV. The resolution is better than 1 MeV.

As seen in Figs. 23 and 24, the proton spectrum shows a pronounced peaking at 130 MeV. This corresponds to an energy of 53 MeV for the three neutrons in their center of mass.

We notice that the spectrum of the proton was not measured below 80 MeV. The reason for this is that from this point down the reaction $\pi^- + He^4 \rightarrow p + 3n + \pi^o$ contributes, and the spectrum of the proton is not uniquely determined by the reaction of interest anymore. This makes the normalization nonunique too. As we will see, this does not create a problem, because all attempts at fitting the data so far yield spectra for the proton that are unquestionably different from that obtained. Furthermore, we can reasonably assume that from the quick drop in cross section observed around 90 MeV, most of the area of the curve concentrates in the

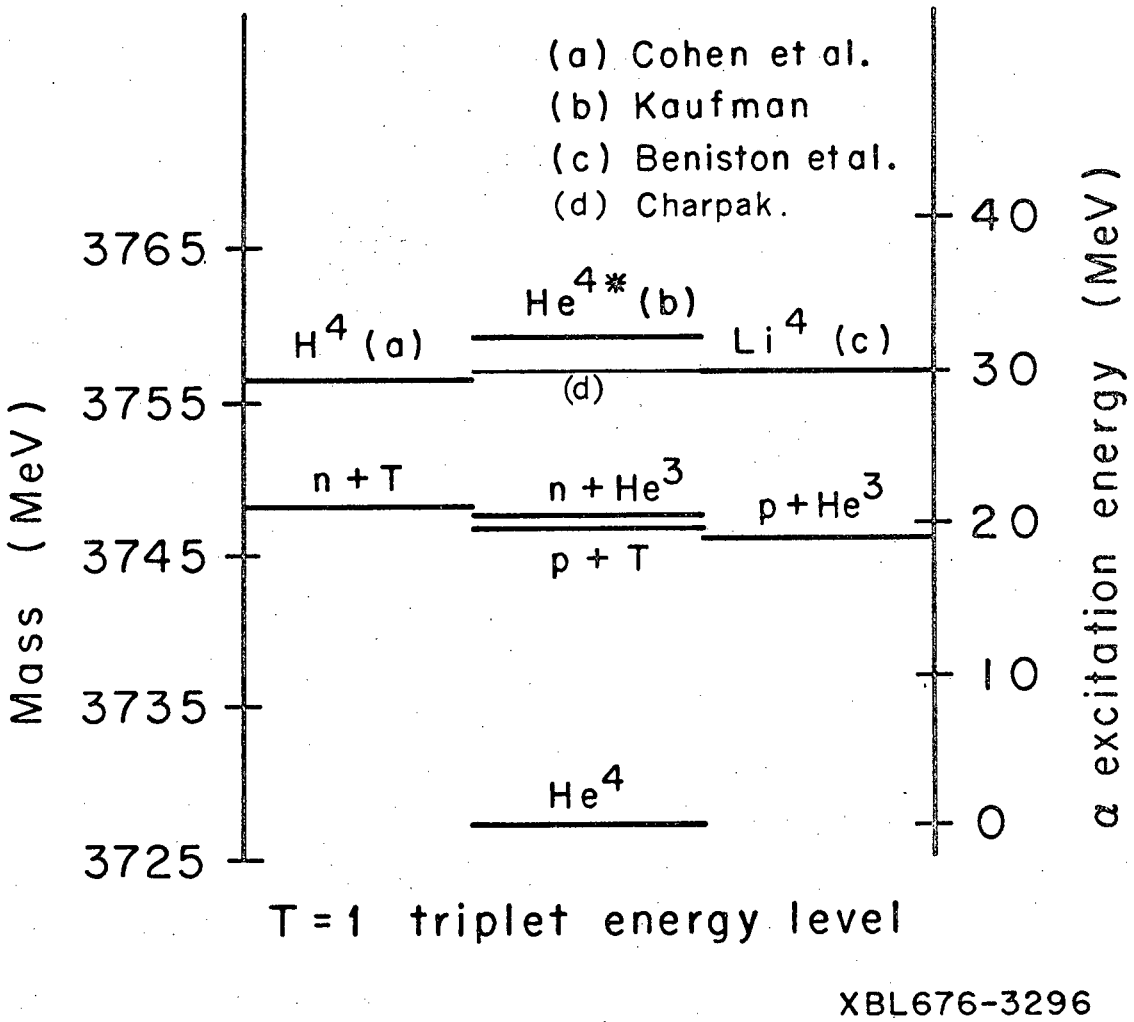

Fig. 25. Some observed levels and thresholds for the A = 4 system.

region measured.

The comparison of immediate interest is made with respect to phase space and phase space aletered by the $^1S_0$ interaction between two of the neutrons in the final state. (The Pauli principle voids the possibility that more neutrons can be in a relative S state.) For this interaction we use standard effective-range theory with a 70-keV scattering length.

The results are shown normalized in two ways. In Figs. 23 and 24 we can compare the spectra with equal areas in the region where measurements were performed; in Fig. 26 we can see the same spectra normalized in such a way that the peaks are at the same height. It is easy to see that the spectra shown differ widely from that observed. We call the reader's attention to the fact that addition of a final-state interaction between the proton and one (or more) of the neutrons will shift its spectrum towards the low-energy end, contrary to what is seen.

At this point, and due to the present lack of knowledge on the problem of handling the interactions of three particles with spin, we attempted some purely phenomenological fits to the behavior of the three neutrons. For this purpose a Breit-Wigner resonance among the three neutrons was assumed. It was found that to obtain moderately successful results we needed to set the three-neutron excitation energy at approximately 45 MeV, using widths of 50 to 70 MeV. In all cases the fit to the data is only partially successful, for the fall in the probability of finding a low-energy proton is much slower for results derived from the Breit-Wigner than is actually observed (Fig. 27).

Another possibility is that we are dealing with a direct reaction mechanism. In this case the high-energy protons would arise from π^- absorption by p-p pairs, producing a proton and a neutron which share the

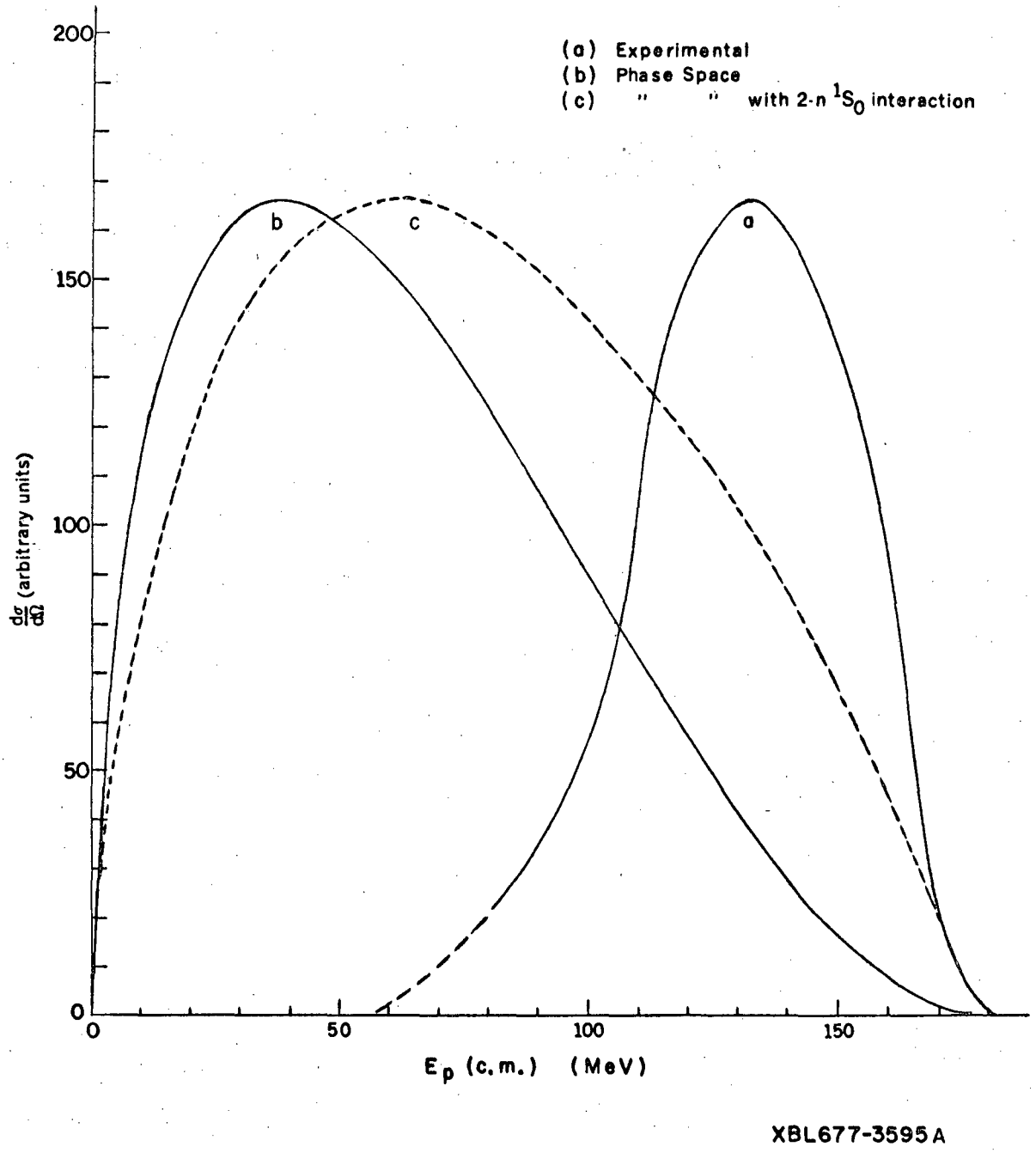

Fig. 26. Some proton spectra.

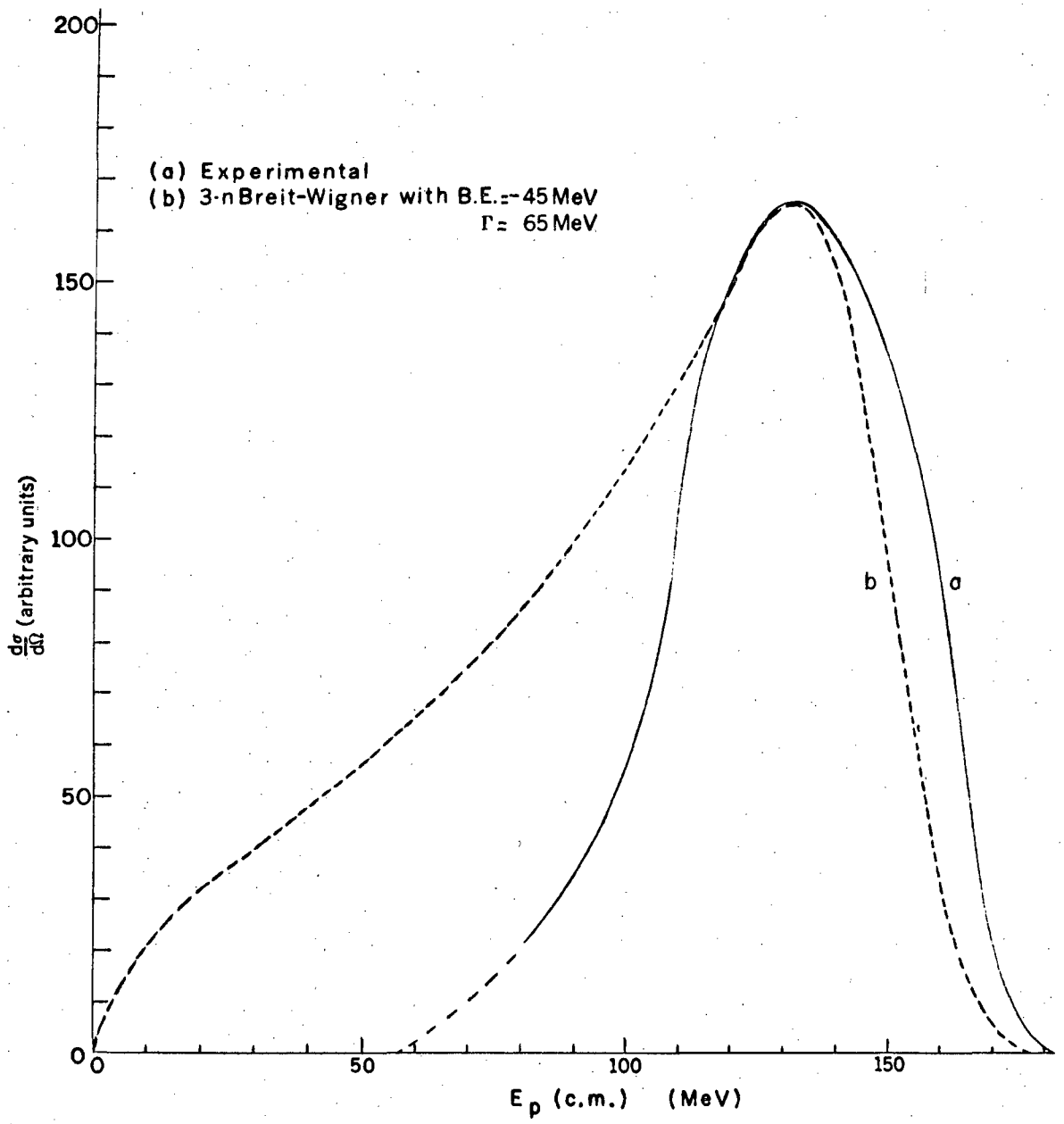

XBL677-3596 A

Fig. 27. Some proton spectra.

energy of the pion, and two other neutrons that are spectators and carry energies of the order of their Fermi momenta in the α nucleus. Were this to be a purely two-body absorption, we would expect the proton to carry about 122 MeV in the c.m. system. This is quite close to the observed most probable proton energy of 130 MeV. The width of this peak (caused by the internal energy of the target nucleons) should be approximately 20 MeV, which is narrower than the observed width. A mechanism may be found that would explain this discrepancy.

A prediction of this model is that n-p abosrption should produce a peak of low-energy protons (0 to 20 MeV). If these protons were to be detected and clearly separated from those produced by the $\pi^0 + p + 3n$, $\pi^- + p + d + n$, and $\pi^- + p + p + n + n$ channels, the direct-reaction model would prove to be a very convincing one. So, together with the latter, the other possibilities open are that when theoretical physicists learn to handle the many-body problem for particles with spin, we will be able to explain the observed effect in terms of a combination of two-body pairwise interactions, or the introduction of three-body forces may become necessary if the previous possibilities fail.

With the data available at present we can give no simple answer. If a model is to be given it will have to be checked against many points, i.e., data will have to be taken at many angles and energies and then the results compared with the predictions of a particular model.[45] This lays emphasis then on further experimentation.

D. $\pi^+ + 4n$ Channel

The 1-MeV resolution achieved in this experiment allowed careful search for a tetraneutron. For a binding energy between -10 MeV and 10 MeV, an upper limit of $1.38 \pm 0.69 \times 10^{-34}$ cm^2/sr-MeV is set for tetraneutron formation under the given conditions.

The π^+ energy spectrum is in agreement with that obtained by Jean et al.[18] in that the best fit corresponds to two neutrons interacting through a $^1S_0$ potential, and the interaction of the other not being strong enough to affect the spectrum appreciably. Our method of measurement does not allow us to determine whether the two neutrons in the $^1S_0$ state were produced by DCX or were spectators.

No effects from the three-neutron interaction seen in Sec. C manifest themselves here. This would follow from the arguments presented by Mitra and Bhasin,[10] that p forces play the dominant role in the three-neutron system, while the kernel for the $^1S_0$-wave part of the force (which predominates in the two- and four-neutron case) is repulsive.[9,10]

ACKNOWLEDGMENTS

I am particularly indebted to Professors Burton J. Moyer and A. Carl Helmholz for their support of this work. Special thanks are due to Dr. Victor Perez-Mendez for the invaluable opportunity for learning I was privileged to enjoy as a graduate student under his guidance.

The author is greatly indebted to many people for the successful completion of this experiment:

To Anthony J. Schaeffer for the excellent and imaginative job he has done in constructing our data-reducing programs, and to Dave Snyder and Leo Vardas for the help they afforded us with the momentum-estimating routines.

To Brownlee Gauld, Johnie Sperinde, and Stephen Williams for the tireless days and nights spent setting up and running this experiment, and to their wives and sweethearts for allowing them to do so.

To Jimmy Vale, Lloyd Houser, and the rest of the 184-inch cyclotron and E. M. crews for their cooperation, help, and cheerful friendliness maintained through all hours of the day.

To Lou Sylvia, Bob Walton, and the Accelerator Technician crews for the excellent, interested, and always competent work they performed during the setup and running.

To Fred Kirsten and the Systems Group, especially Rory Van Tuyl and Jim Ream, for the design, building, and maintenance of the data-acquisition equipment.

To George Constantian and his group, especially Lou Posey and Pete Robinson, for the zeal with which equipment was supplied and repaired.

I also express my thanks to:

Ron Grove for building and helping to maintain the magnetostrictive

wands and delay lines.

Ralph Peters and Bob Fulton of the Engineering Support group for the design of the chambers.

Don Rothfus, Cyclotron Engineering, for the design of the setup.

Arthur Greenberg for the beam design.

Ed McLaughlin, of the Hydrogen-Target Group, and especially Richard Schaeffer and Rene Bollaert and his crew for the design, building, and maintenance of the liquid-hydrogen target.

Pete Watson and the Magnet Test Group for their help in the mapping of the "C" magnet.

Jim Byce and his crew for the excellent and prompt job done on our scintillation counters.

Walt Wenzel and his crew and Adolf Viegelmann for the construction and accurate aligning of the chambers.

Miriam Machlis for typing this thesis and making the best of my handwriting.

This work was done under the auspices of the U. S. Atomic Energy Commission.

APPENDICES

A. Magnetostrictive Readout Chambers

1. Construction

The 8- by 8-in. and 22- by 18-in. chambers were both built by laying 0.006-in. aluminum wires (24 wires to the inch) on lucite and epoxy frames respectively. Each chamber consisted of four such planes. The two inside ones were high-voltage(HV) planes, with their wires at 90 deg to each other and 45 deg to the outside (ground) planes. One of these had its wires running horizontally and the other vertically. This eliminated the ambiguity that arises in locating the position of two sparks when the measurements are performed on coordinates at 90 deg to each other. The first and last wires of each HV plane were connected to the first and last wires of the corresponding ground plane by a resistor chain in series with a capacitor (Fig. 28). In this way each time the chambers fired currents flowed through the wires so connected. This gave rise to two signals on the line. The first signal started two 20-Mc scalers, the second turned one of these clocks off, and the third one turned the other scaler off. The time between the start and end fiducial signals provided a normalizing number that together with the (accurately) known distance between fiducial wires allowed us to determine the coordinate of a spark independently of the factors that may affect the speed of sound on the line, i.e. temperature, tension, composition, density per unit length, etc.

The 49- by 17-in. chambers operated on the same principles, except that they were built from a commercially available copper-nylon mesh that was cut to size, stretched, and glued onto epoxy frames. Each chamber consisted, as before, of the central HV planes and two outside ground planes. The central ones had their wires running horizontally, and wires

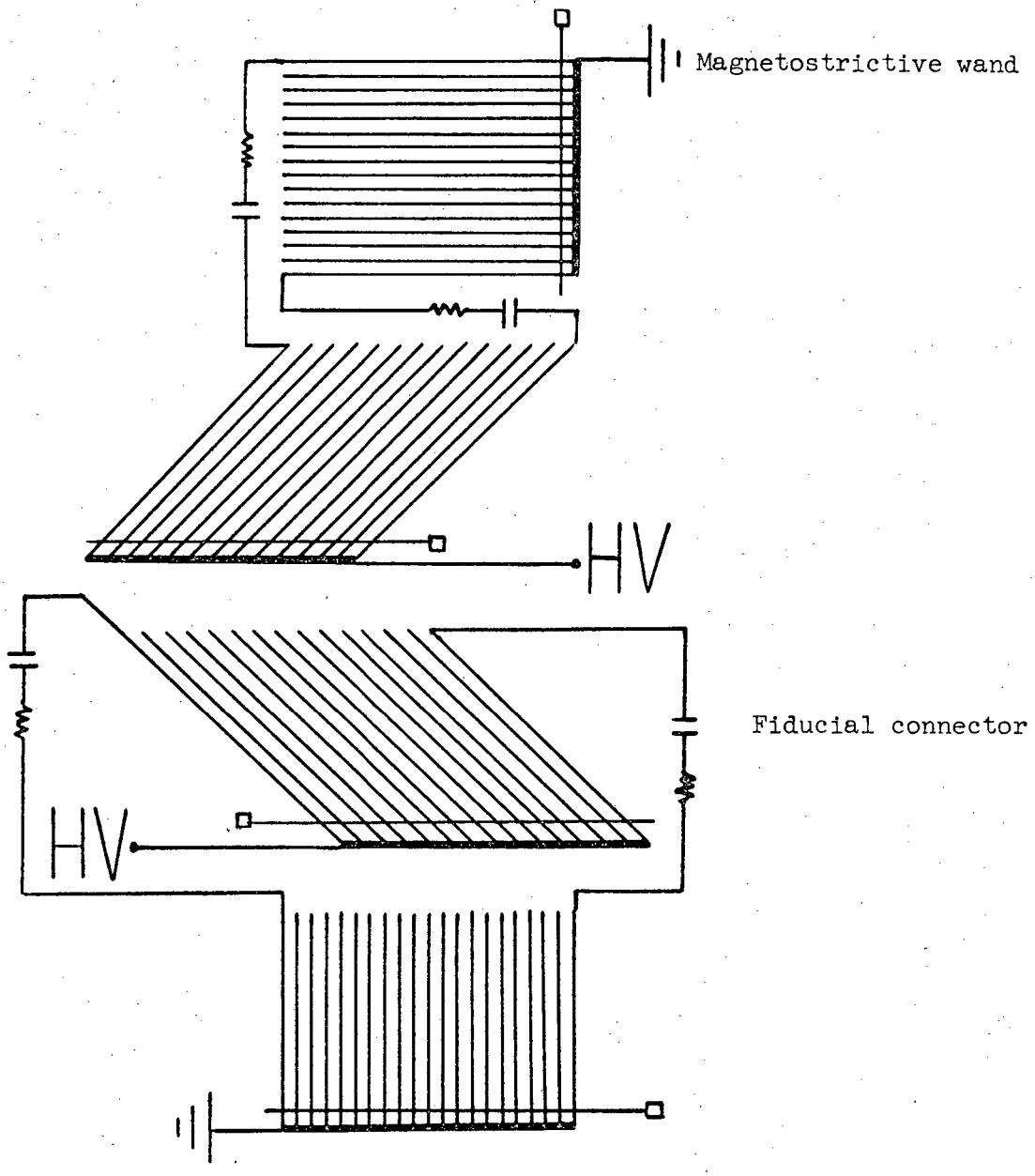

XBL 678-4385

Fig. 28. Schematic diagram of chambers 1 through 4.

in the outside ones were vertical. An additional fiducial wire was provided in the center of the ground planes, so that the long magnetostrictive lines running across these planes could be split in two, with one each for the right and left sides of the chambers respectively (Fig. 29). This allowed for detection of two sparks in each half of the chamber.

As mentioned before, each gap (HV-ground plane combination) was fired by a separate capacitor.

2. Chamber Performance

a. Accuracy. This was checked previous to and after the run. In the first case, four chambers were aligned on the floor of a preparation area and a simple coincidence circuit was provided to fire these chambers when a high-energy cosmic ray went through them.

An event was kept for analysis if each chamber had a spark in it, and the four sparks fell on a line. The data accumulated during the run was used too, for it was much more complete and afforded measurements at a wider range of angles.

By the method already described in Sec. III. A we determined the "best line" between two chambers and then computed ΔR, the distance between the intersection of this line with the plane to the coordinate as measured by the magnetostrictive line.

From simple arguments we can make some predictions about the results of our measurements. The separation between wires was slightly over 1 mm. From the speed of sound in the line (~5000 m/sec) we know that a 20-Mc scaler will yield 4 counts/mm. Given that the magnetostrictive signal picks the "center of gravity" of the current produced by the spark, under ideal conditions the resolution should be $\pm 1/2$ count, (± 0.25 mm) for small angles between the track and the normal to the chamber. This is because

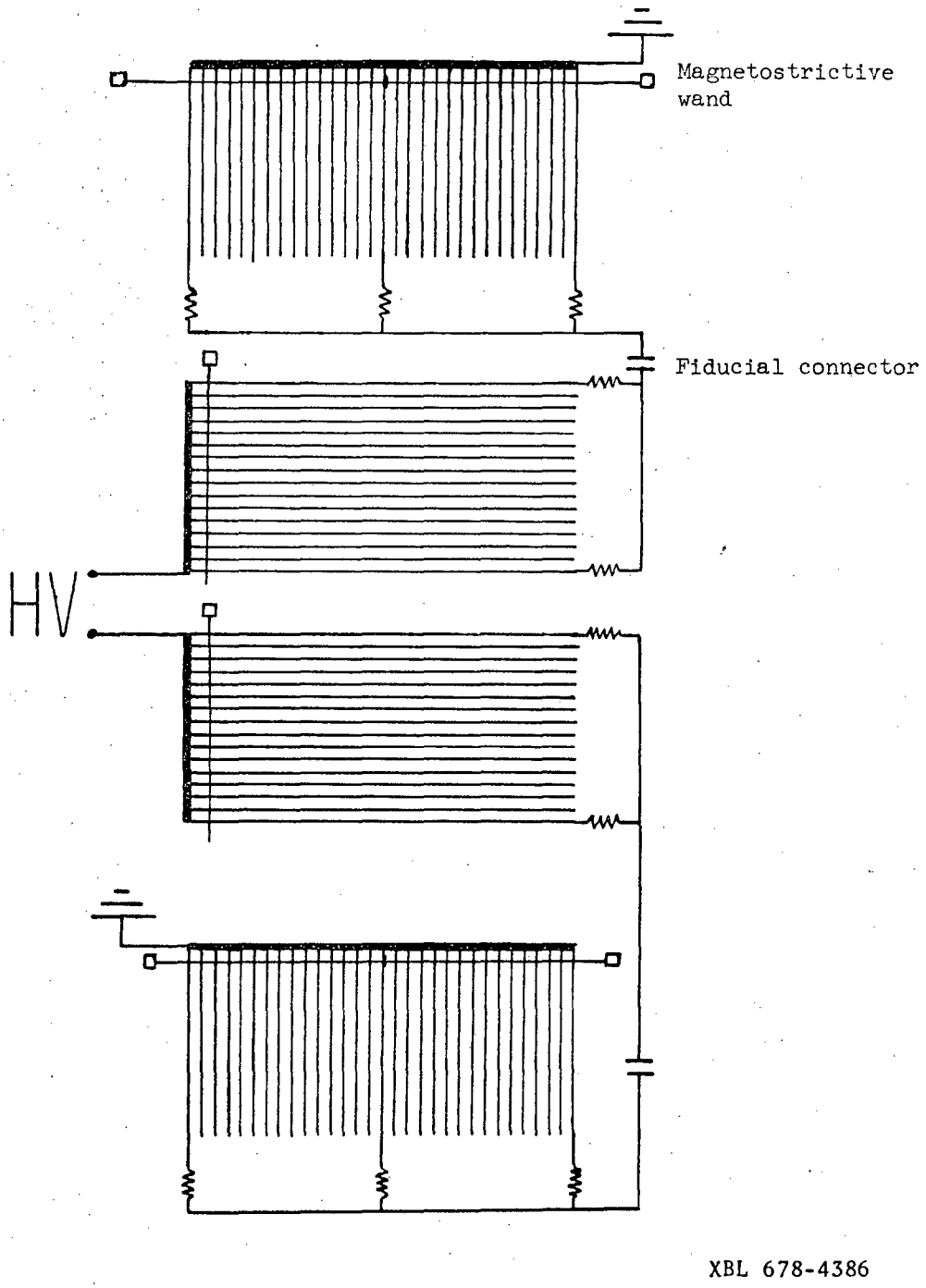

Fig. 29. Schematic diagram of chambers 5 and 6.

for small angles the spark "follows" the ionized track left by the particle. For large angles ($\emptyset \gtrsim 30$ deg) the spark starts on the track but at a certain point leaves it and goes to ground in a direction normal to the plane.

For angles around 45 deg, the sparks just jump straight across the gap. This can be seen in Fig. 30.

Given that the center planes were at negative HV, the spark would start at the point where the particle intersected that plane but arrived at one of the outer planes at ~ gap separation $\times$ cos 45 deg $\approx$ 0.7 cm from where the particle went by, and similarly -0.7 cm in the opposite ground plane.

We expect then that, for tracks at small angles, the spread of ΔR will be slightly over ± 0.25 mm in both the HV and ground planes. On the other hand, if the track is at, say 45 deg, we expect a ΔR peaked about zero with an ~ ± 0.25 mm spread for the HV planes, while ΔR for the ground planes would be peaked about plus or minus 0.7 cm with the same spread as before. If we take a range of angles, then we expect to find a distribution broadened by the angle effect.

Notice too that even for high angles the "best line" found by a least-squares fit to each coordinate will follow the particle's track even though the spark does not (see Sec. III. A.4). Figures 31 through 33 show the results of our measurements.

b. Efficiency. Previous to running we checked chamber efficiency as a function of voltage, and found that optimum running conditions were achieved at approximately 10 kV.

Two efficiencies can be considered here:

(1) Efficiency per plane: For this case we say that a wire plane is

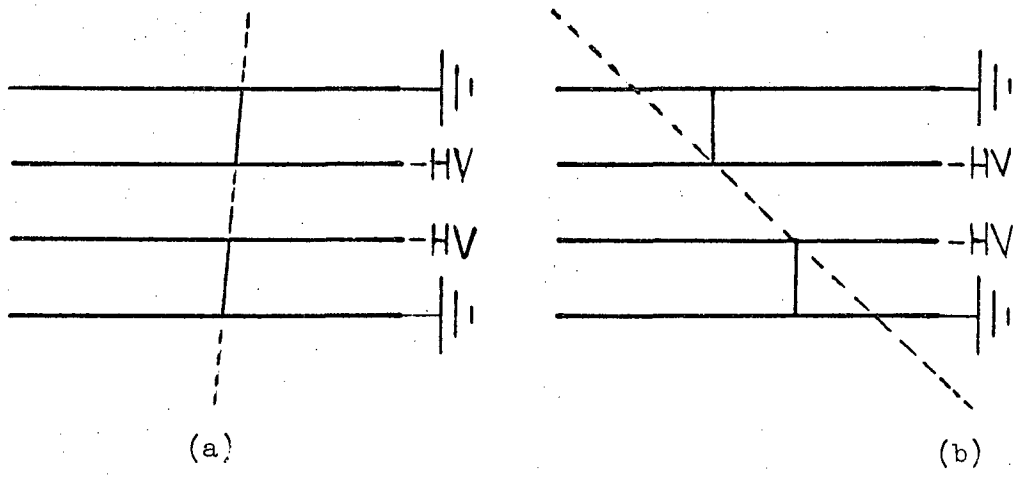

XBL 678-4387

Fig. 30. Particle path and sparks formed for path at (a) small angles and (b) about 45 deg.

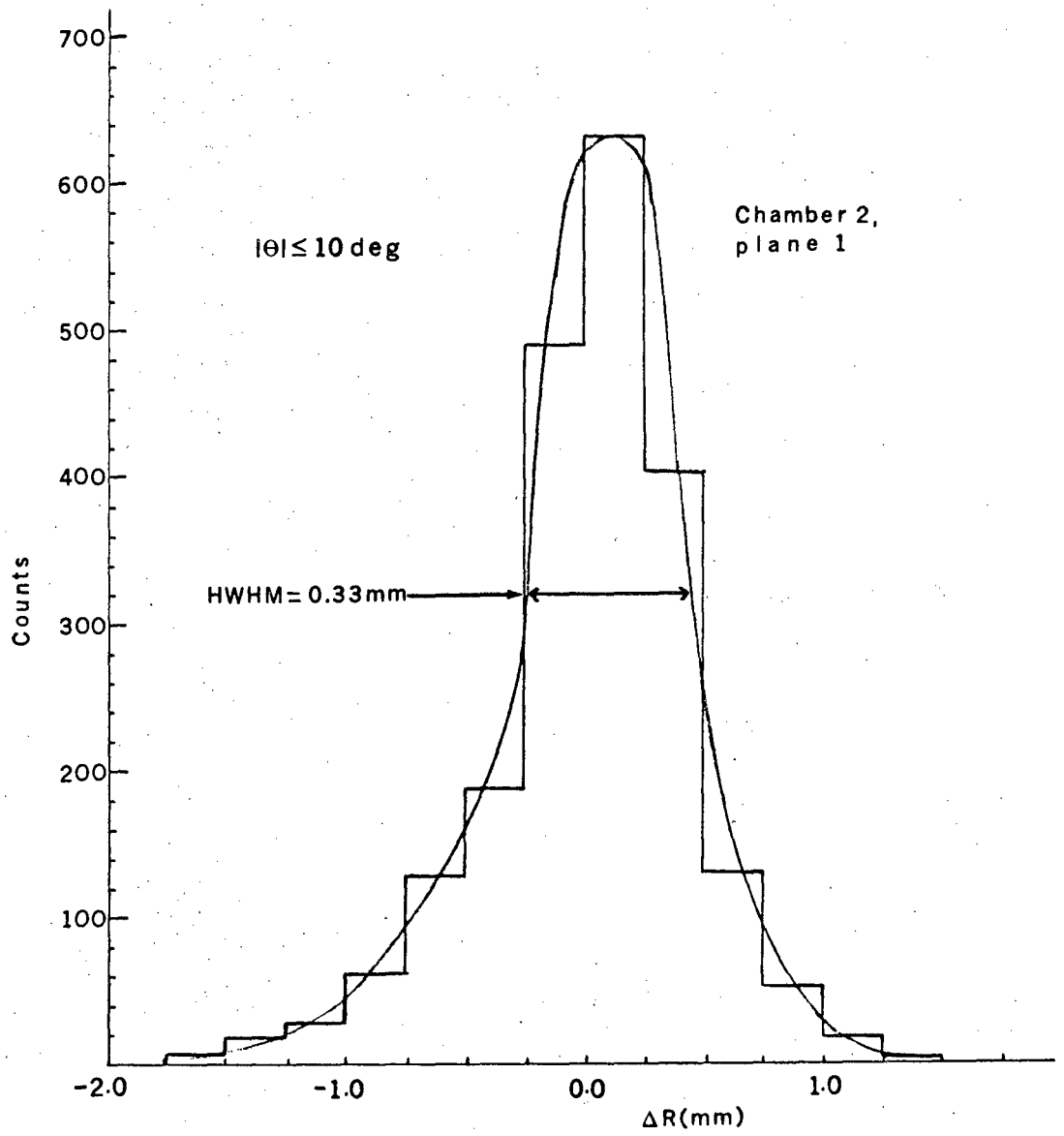

XBL 678-4388

Fig. 31. Deviation of measured coordinate from best line for chamber 2, plane 1.

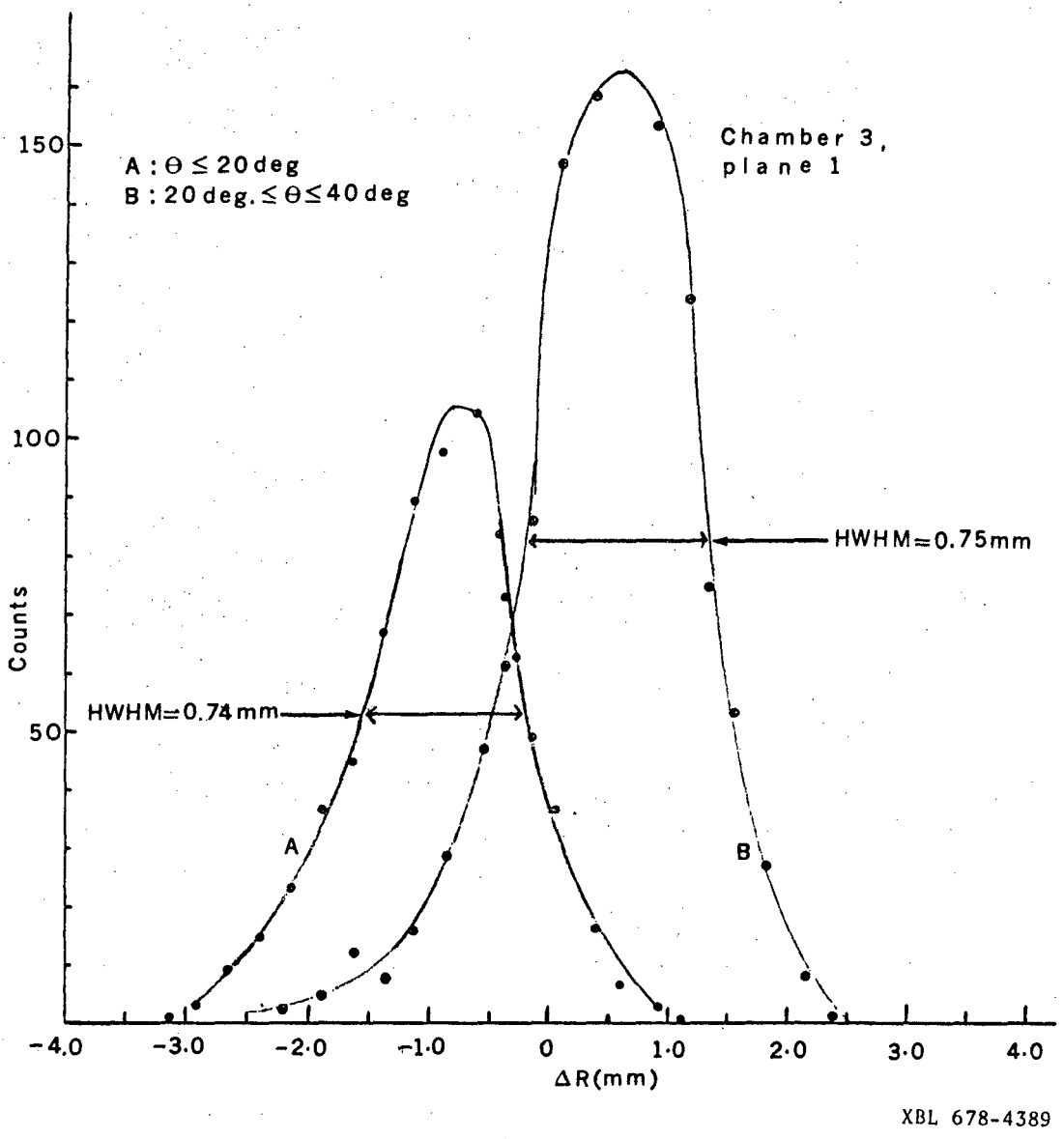

XBL 678-4389

Fig. 32. Deviation of measured coordinate from best line for chamber 3, plane 1.

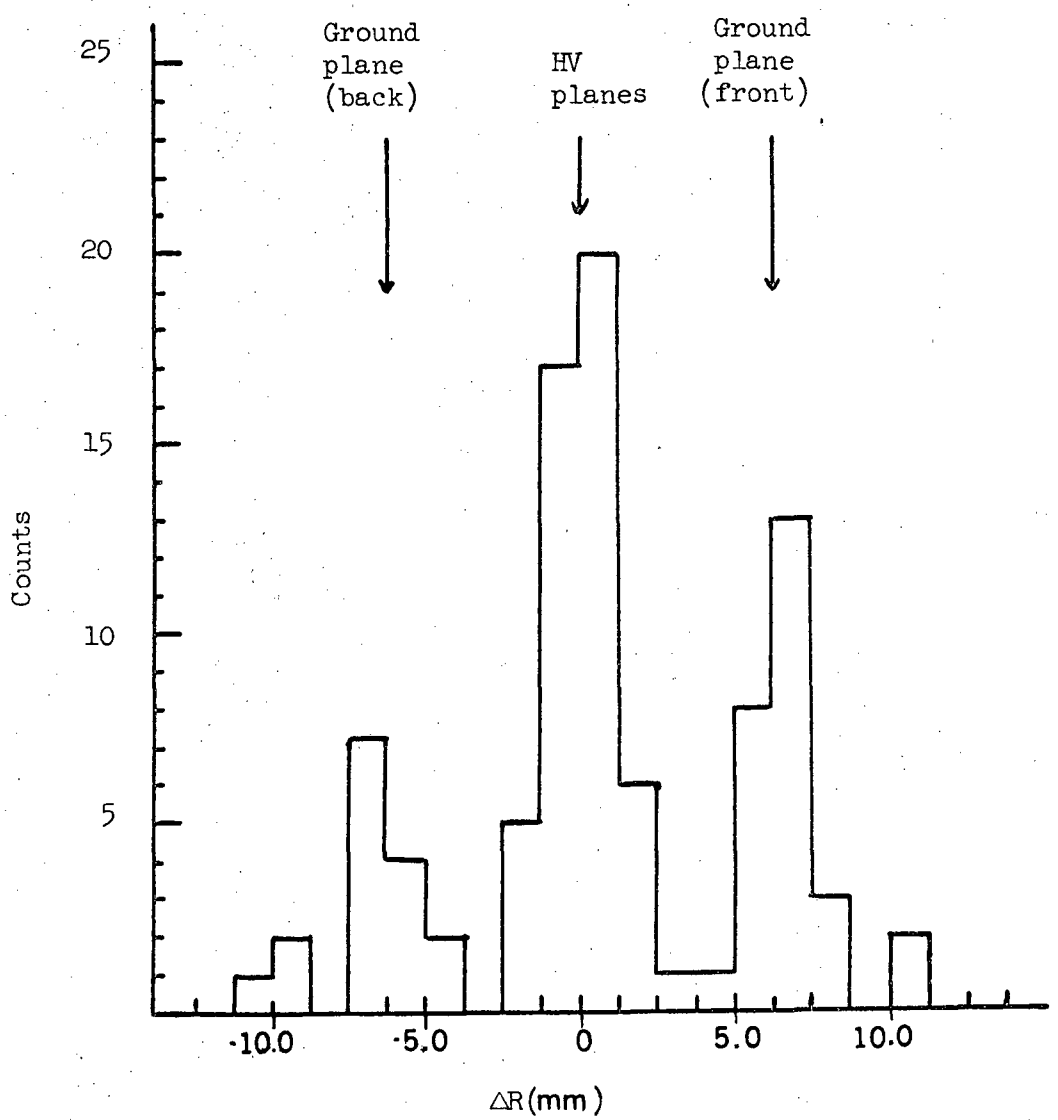

XBL 678-4390

Fig. 33. Deviation of measured coordinate from best line for the four planes in Chamber 5 at θ = 42 $\pm$3 deg.

100% efficient if it contributes a coordinate for every event.

Once the voltage, clearing field, gas mixture, and triggering delay were fixed (as they must be during running), we checked plane efficiency as a function of angle for cases where no more than two sparks occurred. The results are presented in Table AI.

Table AI. Average plane efficiency.

Chamber	$\lvert\theta\rvert \leq 10$ deg	$\lvert\theta\rvert \leq 20$ deg	20 deg $\leq \theta \leq$ 40 deg
Front	98.9%	-	-
Back	-	96.7%	94.8%

(2) Chamber efficiency: The data produced by the chambers will still be useful if not all planes have contributed a coordinate. It is of interest to know the percentage of four-wire, three-wire, and two-wire fits that were present (see Sec. III. A.3), because even though a two-wire fit is enough to determine a point, if we want to resolve the location of two or more sparks we need at least three coordinates. Then we define as 100% efficient a chamber where all events are determined by three- or four-wire fits. The data were taken, as in (1), for cases where no more than two sparks were present, and are summarized in Table AII.

Table AII. Average chamber efficiency.

Chamber	4-wire	3-wire	2-wire	Total
Front	93.2%	6.7%	0.1%	99.9%
Back	87.7%	11.6%	0.7%	99.3%

B. Reduction and Recording of Magnetostrictive-Readout Chamber Data

The signal in the magnetostrictive delay line is picked up by the 200-turn coil-biasing magnet-iron shield assembly described in Ref.43. The signal strength is of the order of 10 mV and is amplified to signals of 1 to 3 V by a preamplifier[42] mounted on the same support that holds the magnetostrictive line. Such an assembly (support, magnetostrictive wire, pickup coil and preamplifier) is called a wand.

The signal output of the wand is processed further as was shown in Figs. 10ab. As we can see, the zero crossover discussed in Sec. II. F.2 eliminates time shifts due to different amplitude signals.

Each event required the timing of the output of 18 wands. If two numbers were desired from each wand, a measurement done with all the data coming in at once (in parallel) would have required 36 scalers. What we did was to load the signals from three wands onto a long magnetostrictive delay line, and then each set of three was timed in series. This cut the number of scalers needed to just 12 (Fig. 34). The operation of these delay lines is discussed in Ref. 42.

The information from the scalers was read onto a buffer store and was sent into a storage scope display. Each wand was displayed horizontally. A short horizontal line was shown for each signal coming from the magnetostrictive line and a vertical short line showed the position as read from the tape. The display was analogue, and checking for the crossing of the horizontal and vertical display lines allowed a check on the performance of the readout, storage and recording systems. It also allowed us to check at a glance that all wands were working properly. We

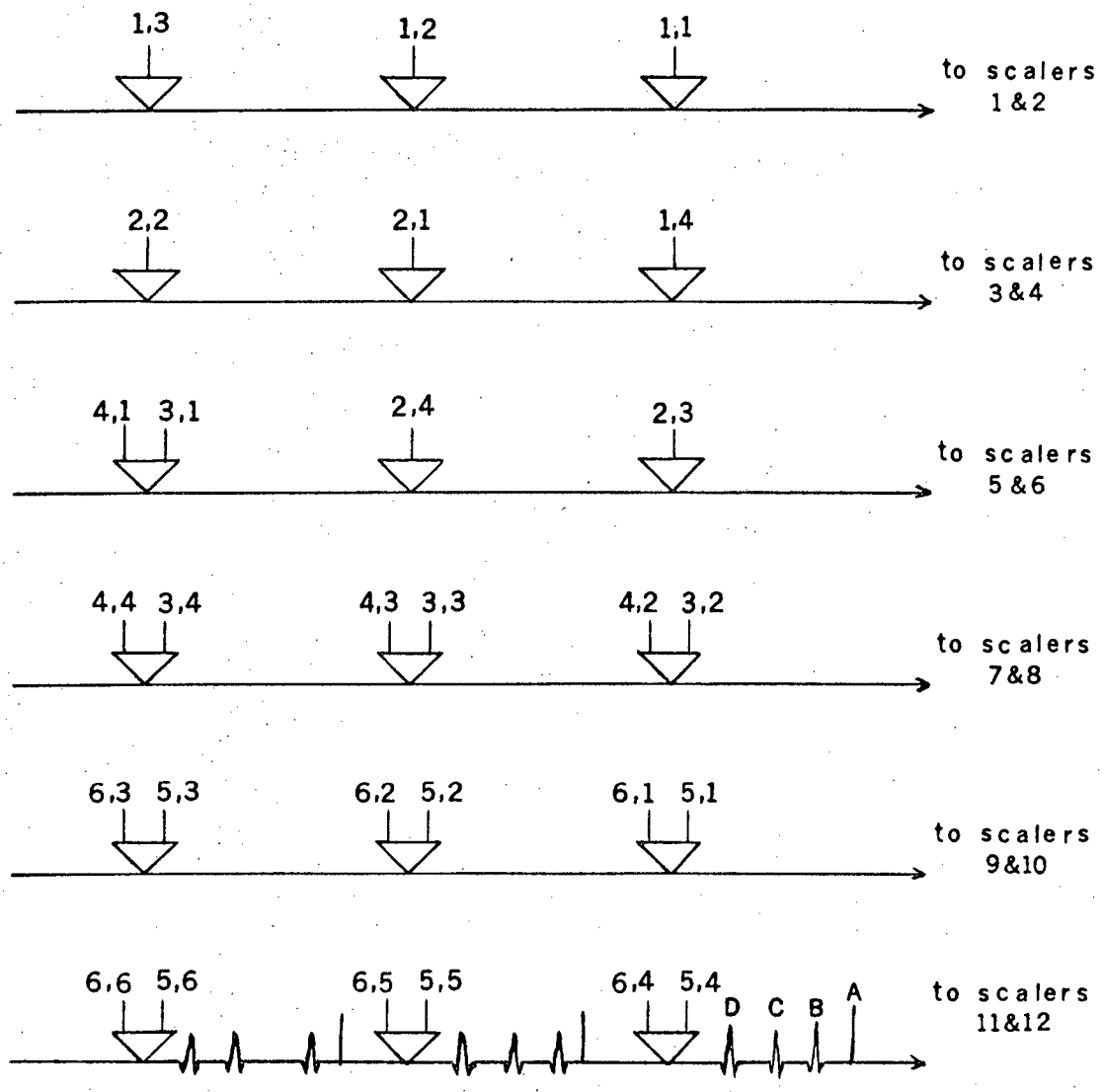

A: Marker pulse (Reset scalers).
B: First Fiducial.
C: Spark.
D: Second Fiducial.
The numbers α,β represent the chamber and plane connected at that point.

XBL 678-4391

Fig. 34. Parallel-series magnetostrictive readout.

had available also a binary light display that allowed us to look at the information going onto tape. A typical display pattern is shown in Fig. 35.

The first four horizontal lines display Chamber 1, the second and third groups of four show Chambers 2 and 3 (or 4) respectively, and the last six display Chamber 5 (or 6).

NOTE: a) Wand Number 1 (from the top) shows a case where only one spark and the fiducial were present.

b) Wand Number 5 shows no sparks. Then the first clock was turned off by the end fiducial and the second clock run up to a high number before being reset (showing as a lone vertical line far towards the right edge of the display).

c) Wand No. 9 shows that two sparks occurred, the fiducial coming in normally (horizontal line). However, with only two scalers available it couldn't be timed and was lost. (The analyzing program supplied a "fiducial" in this case.)

Figure 36 shows α-63, our analog computer. On the left-most rack we have (from the top) two magnetostrictive delay bins, a bin with the 12 scalers, and the display scope with its control bin below. The input panel for the wands is shown at the bottom of that rack. The center rack contains the buffer store and the unit's controls. The rack on the right displays on top the event number, and near the center we can see the binary lights display. To the right can be seen the IBM 729 V tape drive unit modified for use with α-63.

Each tape could be processed in the CDC-6600 computer for immediate information on total performance of the system.

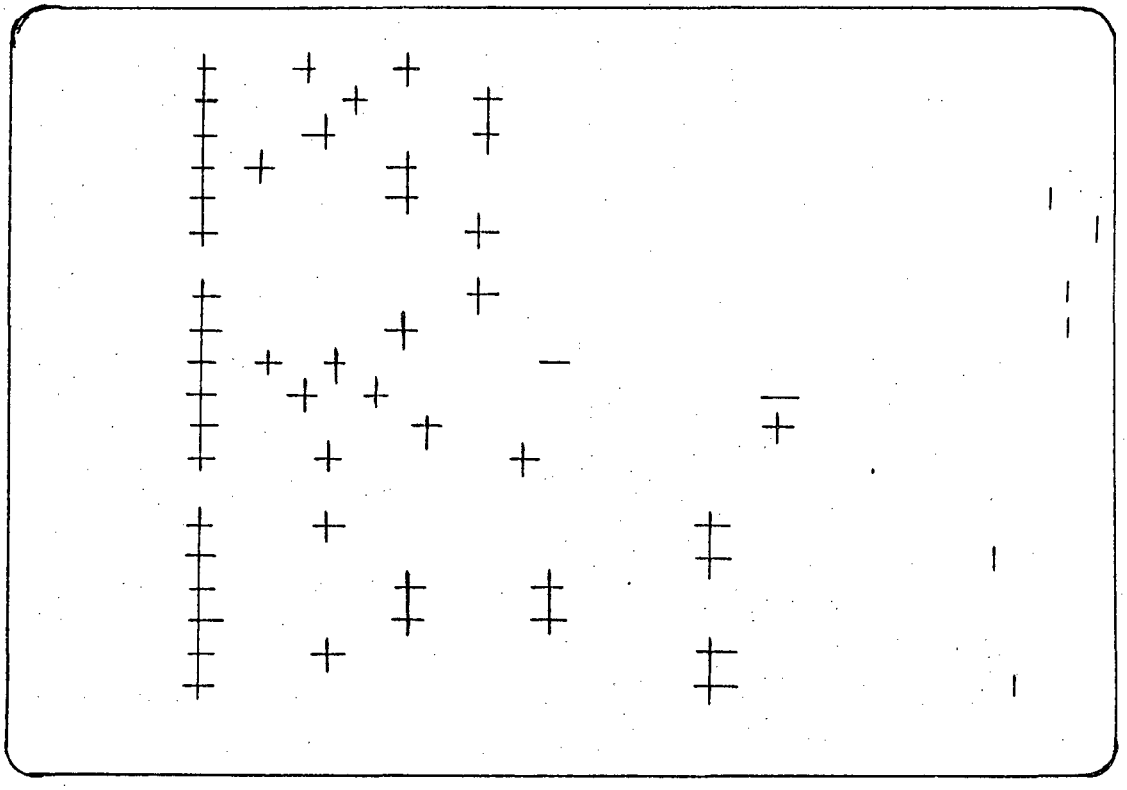

XBL 678-4392

Fig. 35. Typical α-63 oscilloscope display pattern.

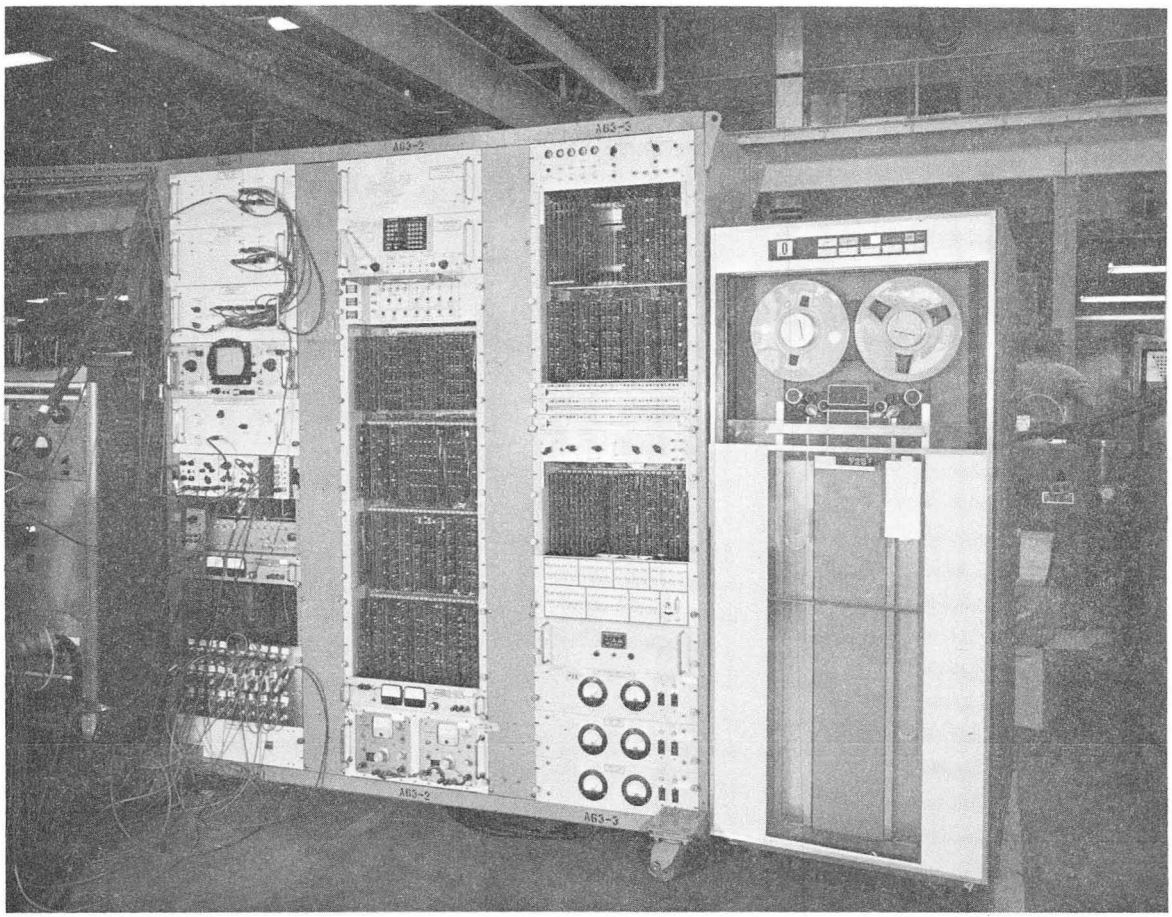

GPR 3281

Fig. 36. The α-63 analog computer.

REFERENCES

1. K. Ilakovac, L. G.Kuo, M. Petravic, and I. Slaus, Phys. Rev. 124 1923 (1961).

2. V. Ajdacic, M. Cerineo, B. Lalovic, G. Paic, I. Slaus, and P. Tomas, Phys. Rev. Letters 14, 442 (1965).

3. E. Baumgartner, H. E. Conzett, E. Shield, and R. J. Slobodrian, Phys. Rev. Letters 16, 105 (1966).

4. R. P. Haddock, R. Salter, M. Zeller, J. B. Czirr, D. R. Nygren, and Tin Maung, Phys. Rev. Letters 14, 318 (1965).

5. Kirk W. McVoy, Phys. Rev. 121, 1401 (1961).

6. K. M. Watson and R. N. Stuart, Phys. Rev. 82, 738 (1951).

7. D. Y. Wong and H. P. Noyes, Phys. Rev. 126, 1866 (1962).

8. V. Ajdacic, M. Cerineo, B. Lalovic, G. Paic, I. Slaus, and P. Tomas, Phys. Rev. Letters 14, 444 (1965).

9. S. T. Thornton, J. K. Blair, C. M. Jones, and H. B. Willard, Phys. Rev. Letters 17, 701 (1966).

10. A. N.Mitra and V. S. Bhasin, Phys. Rev. Letters 12, 523 (1966).

11. K. Okamoto and B. Davies, "A Note on the Existence of n^3," The University of New South Wales (unpublished).

12. A. C. Phillips, "The Non-Existence of the Bound State of Three Neutrons," University of Sussex (unpublished).

13. H. Pierre Noyes, SLAC-PUB-256, January 1967 (unpublished).

14. O. D. Brill, N. I. Venikov, A. A. Kuraschov, A. A. Ogloblin, V. M. Pankratov, V. P. Rudakov, Phys. Letters 12, 51 (1964).

15. R. C. Cohen, A. D. Kanaris, S. Margulies, and J. L. Rosen, Phys. Letters 14, 242 (1965).

16. R. C. Cohen, A. D. Kanaris, S. Margulies, and J. L. Rosen, Phys. Letters 16, 292 (1965).

17. R. E. P. Davis, A. Beretvas, N. E. Booth, C. Dolnick, R. J. Esterling, R. E. Hill, M. Raymond, and D. Sherden, Bull. Am. Phys. Soc. 9, 627 (1964).

18. L. Gilly, M. Jean, R. Neunier, M. Spighel, J. P. Stroot, and P. Duteil, Phys. Letters 19, 335 (1965).

19. Y. C. Tang and B. F. Bayman, Phys. Rev. Letters 15, 165 (1965).

20. Y. C. Tang, Bull. Am. Phys. Soc. 11, 9 (1966).

21. G. Charpak, G. Gregoire, L. Massonnet, J. Saudinos, J. Favier, M. Gusakow, and M. Jean, Phys. Letters 16, 54 (1965).

22. Carl Werntz, Phys. Rev. 133, B19 (1964).

23. D. U. L. Yu and W. E. Meyerhof, Institute of Theoretical Physics, Stanford University, ITP-189, October 1965 (unpublished).

24. W. E. Meyerhof and J. N. McElearney, Nucl. Phys. 74, 533 (1965).

25. R. Frosch, R. E. Rand, M. R. Yearian, H. L. Crannell, and L. R. Suelzle, Phys. Letters 19, 155 (1965).

26. W. E. Meyerhof, Rev. Mod. Phys. 37, 512 (1965).

27. A. de Shalit and J. D. Walecka, ITP-193, SLAC-Pub. 160, Dec. 1965 (unpublished).

28. N. A. Vlasov and L. N. Samoilov, At. Energ. (USSR) 17, 3 (1964) (UCRL-Trans-1183).

29. P. E. Argan, G. C. Mantovani, P. Marazzini, A. Piazzoli, and D. Scannicchio, Nuovo Cimento Suppl. 3, 245 (1965).

30. T. A. Tombrello, C. Miller-Jones, G. C. Phyllips, and J. L. Weil, Nucl. Phys. 39, 541 (1962).

31. M. J. Beniston, B. Krishnamurthy, R. Levi-Setti, and M. Raymond, Phys. Rev. Letters 13, 553 (1964).

32. M. S. Kozodaev, R. M. Suliaev, A. I. Filipovv, and I. U. A. Shcherbakov, JETP 33, 1047 (1957).

33. J. Good, M. Pripstein, and H. S. Goldberg, "Cyclotron Orbits," UCRL-11044, October 1963 (unpublished).

34. Thomas J. Devlin, "OPTIK," UCRL-9727, Sept. 1961 (unpublished).

35. W. A. Wenzel, "Spark Chambers," UCRL-11319, March 1964 (unpublished).

36. V. Perez-Mendez and J. M. Pfab, Nucl, Instr. Methods 33, 141 (1965).

37. V. Perez-Mendez and J. M. Pfab, "Magnetostrictive Readout for Wire Spark Chambers," UCRL-11620, August 1964 (unpublished).

38. F. A. Kirsten, V. Perez-Mendez and J. M. Pfab, "Development of Magnetostrictive Chamber Readouts," UCID-2629, August 1965 (unpublished).

39. Victor Perez-Mendez, "Developments in Magnetostrictive Readouts for Spark Chambers, Proc. 1966 Intern. Conference on Instrumentation for High Energy Physics, Stanford 1966.

40. V. Perez-Mendez, T. J. Devlin, J. Solomon, T. F. Droege, Nucl. Instr. Methods 46, 197 (1967).

41. P. G. Watson, "Brief Description of Operation and Performance Specifications of the LRL Rapid Magnetic Field Mapping System," UCID-1951, August 1963 (unpublished).

42. F. A. Kirsten, K. L. Lee, and J. Lonragan, IEEE Trans. Nucl. Sci. 3, 583 (June 1966); V. Perez-Mendez, R. L. Grove, and K. Lee, "Multiple Tap Magnetostrictive Delay Line Storage," UCID-2839, March 1967.

43. L. Kaufman, V. Perez-Mendez and J. M. Pfab, IEEE Trans. Nucl. Sci. 3, 578 (June 1966).

44. H. Weisberg and D. Snyder, "FEST," UCRL Computer Library report (unpublished).

45. Dr. John Gillespie, Stanford Linear Accelerator Center (private communication) June 1967.

This report was prepared as an account of Government sponsored work. Neither the United States, nor the Commission, nor any person acting on behalf of the Commission:

A. Makes any warranty or representation, expressed or implied, with respect to the accuracy, completeness, or usefulness of the information contained in this report, or that the use of any information, apparatus, method, or process disclosed in this report may not infringe privately owned rights; or

B. Assumes any liabilities with respect to the use of, or for damages resulting from the use of any information, apparatus, method, or process disclosed in this report.

As used in the above, "person acting on behalf of the Commission" includes any employee or contractor of the Commission, or employee of such contractor, to the extent that such employee or contractor of the Commission, or employee of such contractor prepares, disseminates, or provides access to, any information pursuant to his employment or contract with the Commission, or his employment with such contractor.